Cellulose (2025) 32:10027–10049
https://doi.org/10.1007/s10570-025-06823-1

ORIGINAL RESEARCH

Multifunctionality of carboxyl groups carried by cellulose nanocrystals for mechanical and conductive properties of acrylic-based hydrogels—mechanism study

Tao Song · Qiang Wang · Tingting Han · Alain Dufresne · Fernanda Andrade Tigre da Costa · Duclerc Fernandes Parra

Received: 8 April 2025 / Accepted: 15 October 2025 / Published online: 27 October 2025

Abstract In this work, an integrated strategy was proposed for preparing hydrogel based on acrylic acid (AA) and sodium alginate (SA) by adding TEMPO-oxidized cellulose nanocrystals (TOCNs) with different carboxylic groups (–COOH) contents. The addition of TOCNs and increase of its contents in poly(acrylic acid) (PAA)/SA hydrogel systems played a multifunctional role by which the mechanical properties and ionic conductivity of PAA/SA hydrogels were significantly affected and enhanced. TOCNs with their abundant –COOH groups disperses SA and AA in the hydrogel precursor solution for forming a uniform semi-interpenetrating network. It also provides more hydrogen bonds with SA and AA, and results in high modulus of the final hydrogel. Accordingly, the as-prepared hydrogels showed simultaneous good compressive (1.41 MPa at compressive strain of 70%) and tensile (365 kPa strength at fracture strain of 628%) stresses, excellent swelling rate (2509%), good transparency (86.3%) and conductivity (0.229 S m^{-1}). The work confirmed the important roles of –COOH in the TOCNs played in the construction and properties of the hydrogel, and the hydrogels may find great potential applications in the fields of flexible wearable sensors benefits by excellent natural biocompatibility from all the raw materials used.

Supplementary Information The online version contains supplementary material available at https://doi.org/10.1007/s10570-025-06823-1.

T. Song (✉) · Q. Wang
State Key Laboratory of Biobased Material and Green Papermaking, Qilu University of Technology, Shandong Academy of Sciences, Jinan 250353, People's Republic of China
e-mail: songt@scut.edu.cn

T. Song
State Key Laboratory of Advanced Papermaking and Paper-Based Materials, South China University of Technology, Guangzhou 510640, People's Republic of China

T. Han (✉)
Guangzhou Key Laboratory of Sensing Materials & Devices, Centre for Advanced Analytical Science, School of Chemistry and Chemical Engineering, c/o School of Civil Engineering, Guangzhou University, Guangzhou 510006, People's Republic of China
e-mail: tinghan@gzhu.edu.cn

A. Dufresne · F. A. T. da Costa
CNRS, Grenoble INP, LGP2, University Grenoble Alpes, F-38000 Grenoble, France

F. A. T. da Costa · D. F. Parra
Nuclear and Energy Research Institute, IPEN–CNEN/SP, Av. Prof. Lineu Prestes, 2242, Cidade Universitária, São Paulo, SP CEP 05508-000, Brazil

Graphical abstract

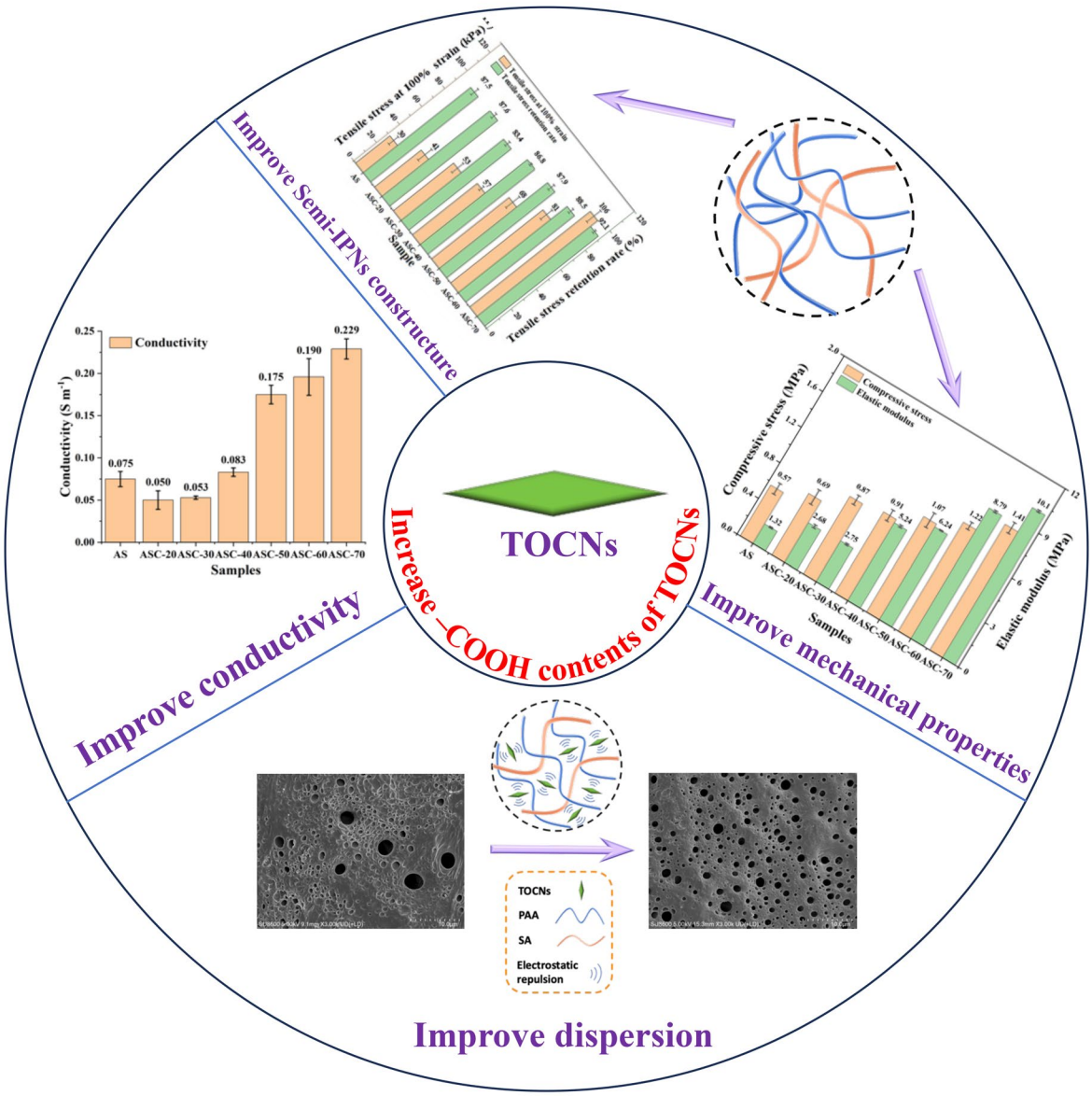

Keywords Conductivity · Mechanical properties · Multifunction · Polyacrylic acid · Sodium alginate · TEMPO-oxidized cellulose nanocrystals

Introduction

With today's focus on many high-tech smart devices, such as artificial intelligent facilities, telemedicine diagnosis, human–machine interfaces, among others, researchers worldwide have become increasingly interested in the innovative design of flexible and wearable electronic sensors. Compared to the most commonly used conductive materials for sensors, e.g. metals (Schazmann et al. 2010; Bandodkar et al. 2014) and conductive polymers (Wang et al. 2018; Ke et al. 2021), conductive hydrogels have attracted more and more interests due to their far superior properties

compared to the two aforementioned conductive materials, including excellent bendability and skin affinity, function tunability, reliable ionic conductivity and easy fabrication, among others (Liu et al. 2020; Pinelli et al. 2020; Zhang et al. 2020; Ling et al. 2021; Ho et al. 2022). Thereby, conductive hydrogels have been considered a more ideal material for assembling flexible and wearable electronic sensors.

Hydrogels are typically soft and moist polymeric materials with 3D-network structures, which can hold large amounts of liquids while still remaining stable and insoluble (Brannon-Peppas and Harland 1990). Conventionally, they are formed by cross-linking polymers through physical, ionic or covalent interactions (Yang et al. 2014; Wieduwild et al. 2015; De Koker et al. 2016), using mainly synthetic petroleum-based polymers as substrates, such as poly(2-hydroxyethyl methacrylate) (pHEMA) (Wichterle and Lim 1960; Buwalda et al. 2014), poly(ethylene glycol) (PEG) (Buwalda et al. 2014), poly(vinyl alcohol) (PVA) (Chen et al. 2020; Fang et al. 2023), poly(acrylic acid) (PAA) (Li et al. 2020; Luo et al. 2024a) and poly(acrylamide) (PAM) (Kong et al. 2018; Godiya et al. 2019). Among these synthetic polymers, PAA, synthesized by polymerization of acrylic acid (AA), not only exhibits better biocompatibility (Joshi et al. 2013; Koehler et al. 2017; Jeong et al. 2020), but also carries a large amount of hydrophilic –COOH groups, which can provide a moisture-rich cross-linked network for ion-conductive hydrogels, endowing PAA-based ion-conducting hydrogels with high ionic conductivity (Jiao et al. 2021a, b; Zhang et al. 2021; Ling et al. 2022). However, simultaneously possessing competitive mechanical strength and fatigue-resistance as well as conductive properties remains a challenge for pure PAA conductive hydrogels (Fan et al. 2013; Li et al. 2014; Chen et al. 2019), especially for its compressive strength. Consequently, they are often damaged or destroyed when high external compressive forces are applied. This greatly inhibits their application as strain and pressure sensors for pressure sensing, e.g., in the detection of human diseases, such as the preliminary screening of patients suffering from flat feet (Ling et al. 2021).

Formation of double or multiple networks have been reported in many previous works that can improve the compressive strength and anti-fatigue properties of hydrogels by regulating intermolecular or intramolecular interactions (Chen et al. 2015; Xu et al. 2016; Zhang et al. 2016; Lin et al. 2019; Dhand et al. 2021; Hao et al. 2021). Among the strategies for forming multi-network hydrogels, inter-penetrating network (IPNs) is an important one in which polymer network(s) (IPNs) or entangled linear polymer(s) (semi-IPNs) interpenetrate into the other crosslinked networks (Gong et al. 2003; Daniele et al. 2014; Dashtebayaz et al. 2019), offering better control over the chemical composition and the final properties of the resulting materials (Dragan et al. 2014; Aminabhavi et al. 2015; Maleki et al. 2016). The mechanical properties and durability of hydrogels formed by IPNs can be enhanced over those composed of a single component, because their structure can only be decomposed or degraded by breaking up the whole network.

Furthermore, among the natural polysaccharides carries a large amount of hydrophilic–COOH group for ion-conductive hydrogel fabrications, sodium alginate (SA) and carboxylated nanocellulose (CNC–COOH) have attracted a lot of attentions in the current years (Qiao et al. 2019; Li et al. 2022; Luo et al. 2024a and b). SA is one of the natural anionic polysaccharides which can be fractionated on a large scale from seaweeds. Its structure is composed of (1→4) linked β-D-mannuronic acid and α-L-guluronic acid residues (Draget and Taylor 2011). SA is an ideal polymer used for the formation of conductive hydrogels, which usually exhibit good ionic conductivity owing to a large number of conducting ions on the SA structure (Qiao et al. 2019). SA and PAA have been combined to form IPN hydrogels (Li et al. 2022). In the hydrogel structure, linear SA penetrates the free radical polymerized AA (PAA) network to form a semi-IPN. However, AA and SA in the aqueous phase are prone to hydrogen bonding, van der Waals forces and other intermolecular interaction forces, resulting in easy agglomeration, significantly affecting the network structure formed by SA and PAA (Li et al. 2022). On the other hand, CNC–COOH has mainly be prepared by TEMPO-mediated oxidization (Isogai et al. 2011) and, in recent years, also developed by poly-carboxylic acid hydrolysis (Ji et al. 2019; Luo et al. 2021; Cen et al. 2022; Shi et al. 2024). CNC–COOH has excellent biocompatibility, natural extremely high Young's modulus, high specific surface area and high surface activity (Hamad 2006; Kobayashi et al. 2014), which have been widely applied as an extraordinary additive,

especially for enhancing the mechanical properties of hydrogels (Liu et al. 2017; Lin et al. 2019; Xiao et al. 2021). More than this, charged CNCs has also shown efficient dispersing ability and applied in various reported systems, e.g. dispersion of CNTs (Mougel et al. 2016; Wang et al. 2025) and AgNPs (Tang et al. 2015), Pickering emulsions (Li et al. 2018; Guo et al. 2023), etc.

All above inspired us that we could take CNC–COOH as a systemic dispersant for solving the agglomeration problem of SA or/and AA, simultaneously as a mechanical enhancing agent for improving the mechanical properties of SA- or/and AA-based hydrogels, and as a –COOH donor for providing more hydrogen bonds with SA and AA to create a uniform multi-semi-IPNs and providing more conductive ions. Among the multifunction of CNC–COOH mentioned above, the charged –COOH groups on CNC–COOH have been hypothesized to probably play the main role in affecting the hydrogel structure and, correspondingly in its properties (Luo et al 2024a and b). To further confirm this, the effect and detailed mechanism of –COOH in CNC–COOH on the hydrogel structure and properties have to be verified or clarified. Therefore, in the present work, a series of carboxylated cellulose nanocrystals (TOCNs) with different –COOH contents were prepared by TEMPO-mediated oxidization and used for enhancing the mechanical and conductive properties of PAA/SA hydrogel. To confirm the multifunctional role and mechanisms of –COOH of TOCNs in the hydrogel, the chemical formation, morphological structure, mechanical and ionic conductivity properties of hydrogels made with TOCNs addition and their varied –COOH contents were primarily and systematically evaluated. Benefiting from the fact that all raw materials used in the present work have great biocompatibility, the hydrogel has great potential application prospects in the field of flexible wearable sensors, such as for analyzing the deformation trajectory of objects and detecting human health.

Experimental

Materials

Acrylic acid (AA, AR, > 99%) and NaOH (≥ 95%) were purchased from Shanghai Macklin Biochemical Co., Ltd (Shanghai, P.R. China). $(NH_4)_2S_2O_8$ (APS, AR, ≥ 98%) and N, N′-Methylenebisacrylamide (MBA, ≥ 99%) were supplied by Aladdin Biochemical Technology Co., Ltd (Shanghai, P.R. China). Sodium alginate (SA, AR, 98%) was provided by Yuanye Biological Technology Co., Ltd (Shanghai, P.R. China). The average molecular weight of SA was ~ 200 kDa, and the ratio of mannuronic and guluronic units (M/G) was ~ 1.56. 2,2,6,6-Tetramethyl-1-piperidinyloxy (TEMPO, 98%), microcrystalline cellulose (MCC, 25 μm in particle size), NaBr (AR, 99%) and NaClO (AR, 6 ~ 14%) used to produce TOCNs were all purchased from Shanghai Macklin Biochemical Co., Ltd (Shanghai, P.R. China).

Chemical and analytical methods

Preparation of TOCNs

Carboxylated cellulose nanocrystals (TOCNs) used for hydrogel production were prepared by TEMPO-mediated oxidation method in lab scale with minor modifications (Barbash et al. 2022). Briefly, 10 g of MCC was suspended in 500 mL of deionized water (DI-water) by stirring at 300 rpm (MR Hei-Tec, Heidolph, Germany). Followed this, the MCC suspension was mixed with 100 mL of solution containing 0.17 g of TEMPO and 2 g of NaBr, and kept stirring at 300 rpm for 2 h. TEMPO-mediated oxidation of MCC suspension started by adding 10 mL of saturated NaClO reagent each time while the suspension was continuously stirred at room temperature. After adding each 10 mL of NaClO, the pH remained constant at 10.5 by adding 0.5 M of NaOH solution until no more alkali consumption was observed, indicating that the reaction was completed. The total volumes of added NaClO reagent were 20 ~ 70 mL to control the –COOH contents of TOCNs.

The sediment of the TEMPO-oxidized CNCs was obtained after thoroughly washing with distilled water by centrifugation four times at 4000 rpm (Allegra X-30, Beckman Coulter, American) to remove unreacted chemicals. It was then diluted to 1.0 wt% with DI-water and mechanically fibrillated by a high-pressure microfluidizer (MINI, Noozle, Shanghai, China) at 14,000 psi for five cycles to obtain TOCNs suspensions. The suspension was then dialyzed with a membrane (Mw cut-off of 14 kDa) in DI-water until the conductivity of the permeate approached that of DI-water. The dialyzed TOCNs

suspension was concentrated using a rotary evaporation (Hei-VAP Value Digital, Heidolph, Germany) to remove some of the water, and the TOCNs solid powder was then obtained by freeze-drying (FDu-1200, EYELA, Japan) and stored in a refrigerator at 4 °C. The TOCNs with different –COOH contents were named as TOCN-20 ~ 70 based on the total amount of NaClO solution (mL) added for oxidation (Table 1).

Preparation of hydrogels

Hydrogels were prepared based on our previously reported process (Luo et al. 2024b). Specifically, 8 g of SA solution (2.5 wt%) was slowly mixed with 2 g of pre-dispersed TOCNs-suspension (1.0 wt%) under stirring at 500 rpm (MR Hei-Tec, Heidolph, Germany). After adding 10 mL of DI-water, the mixture was stirred under the same speed for 30 min and a homogeneously dispersed SA-TOCNs mixture was obtained. Following, 7 g of AA was slowly added to the SA-TOCNs mixture under stirring at 800 rpm and kept stirring at room temperature for 30 min. Then, 7 mg of MBA (as the cross-linking agent) and 70 mg of APS (as the initiator) were added to the mixture, and kept stirring at 800 rpm for another 30 min to well-disperse the mixture. The final mixtures after the removal of air bubbles were immediately transferred to a polytetrafluoroethylene mold with cover and heated in an oven (BPG-9070A, Shanghai Yiheng, P.R. China) at 60 °C for the free radical polymerization reaction. After 3 h, hydrogel samples with two different shapes (cubic and dumbbell) were formed, and named ASC-20 ~ 70 based on the total amount of NaClO solution (mL) added for oxidation (Table 2).

Table 1 Raw material composition of preparing TOCNs

Sample code	MCC (g)	TEMPO (g)	NaBr (g)	Saturated NaClO (mL)
TOCN-20	10	0.17	2	20
TOCN-30	10	0.17	2	30
TOCN-40	10	0.17	2	40
TOCN-50	10	0.17	2	50
TOCN-60	10	0.17	2	60
TOCN-70	10	0.17	2	70

Characterizations

Carboxyl content of TOCNs

The carboxyl content of TOCNs samples was determined by conductometric titration. Briefly, about 0.1 g of freeze-dried TOCNs was well dispersed in a mixture of DI-water (50 mL) and NaCl solution (0.01 mol/L, 5 mL) assisted with ultrasonication (JY99-IIDN, Scientz, China) for 10 min (900 W at a frequency of 20 kHz with 5 s intervals). Following, HCl solution (0.15 mol/L) was added to adjust the pH of the suspension at 2.5 ~ 3.0. After that, the suspension was titrated using NaOH solution (0.1 mol/L) by adding 50 μL in 25 s intervals. The conductivity initially decreased and then remained stable until an increase was observed. Then, the content of carboxylic groups was calculated based on the following Eq. (1).

$$B = \frac{c \times \left(V_2 - V_1\right)}{m} \tag{1}$$

Table 2 Summary of the characteristics of TOCNs with different –COOH contents

Samples	Length (nm)	Aspect ratio	–COOH (mmol/g_{TOCNs})	Zeta-potential (mV)		CrI (%)
				TOCNs	SA-TOCNs	
MCC	–	–	–	–	–	75.6 ± 1.07
TOCN-20	709.6 ± 232.4	30.7	0.43 ± 0.04	− 35.59 ± 0.24	− 55.66 ± 2.15	83.3 ± 1.13
TOCN-30	667.0 ± 201.1	27.7	0.54 ± 0.02	− 42.55 ± 0.10	− 64.52 ± 1.03	81.5 ± 0.75
TOCN-40	514.2 ± 167.8	23.5	0.67 ± 0.02	− 45.39 ± 0.27	− 69.54 ± 1.67	80.1 ± 0.63
TOCN-50	691.3 ± 133.6	24.1	0.74 ± 0.04	− 50.30 ± 0.28	− 78.37 ± 0.96	81.5 ± 1.32
TOCN-60	488.4 ± 104.5	22.2	0.86 ± 0.06	− 55.68 ± 0.17	− 84.83 ± 0.27	78.5 ± 2.47
TOCN-70	380.5 ± 88.7	19.1	1.02 ± 0.01	− 62.28 ± 0.06	− 96.66 ± 1.83	76.7 ± 2.63

where B (mmol/g_{TOCNs}) is the carboxylic group content of TOCNs, c (0.1 mol/L) is the concentration of NaOH, V_1 and V_2 (mL) are the volumes of NaOH solution consumed at the starting point and end point of the titration, respectively; m (g) is the mass of TOCNs.

Morphological structure of TOCNs

The morphological structure of TOCNs was observed by atomic force microscopy (AFM, Nanoscope III, Veeco, USA) in tapping mode. Before characterization, a drop of diluted TOCNs suspension (concentration of ca. 0.05 wt‰) was dropped on the surface of a clean mica film and dried naturally in a ventilated place. The obtained AFM images were analyzed with the NanoScope Analysis 1.5 program. About 80 ~ 150 particles were randomly selected from each sample image to determine the average diameter and length of TOCNs.

Crystallinity of TOCNs

X-ray diffraction (XRD) patterns of all TOCNs samples were recorded on an X-ray diffractometer (Xpert Powder, Panalytical, Netherlands) equipped with Cu-Kα radiation generated under an operating voltage of 40 kV and a filament current of 40 mA. Scattered radiation was detected for angles (2θ) ranging from 5° to 60° at a scan rate of 12°/min. The calculation of the crystallinity index (CrI) for each sample was based on the following Eq. (2), and the CrI of each TOCNs was obtained from three parallel samples' tests:

$$CrI(\%) = \frac{I_{200} - I_{\mathrm{am}}}{I_{200}} \quad (2)$$

where I_{200} is the maximum peak intensity of the lattice diffraction (200) plane and I_{am} is the minimum intensity between the planar reflections (200) and (110).

Zeta-potential of TOCNs and SA-TOCNs suspensions

Before tests, the TOCNs suspensions were diluted to 0.15 wt% and ultrasonicated (JY99-IIDN, Scientz, China) for 15 min (900 W at a frequency of 20 kHz with 5 s intervals). For SA-TOCNs suspension preparation, TOCNs suspensions with concentration of 1.0 wt% were pre-dispersed by ultrasonication, after which, 8 g of SA solution (2.5 wt%) was slowly added into TOCNs suspension under stirring at 500 rpm (MR Hei-Tec, Heidolph, Germany). After adding 10 mL of DI-water, the mixture was stirred under the same speed for 30 min and a homogeneously dispersed SA-TOCNs mixture was obtained.

A dynamic light scattering nanoparticle analyzer (SZ-100Z, Horiba, Japan) was then applied to determine the Zeta-potential of both TOCNs and SA-TOCNs suspensions. The measurement of each sample was carried out for three times using the graphite electrode pool.

Fourier transformed infrared spectroscopy (FT-IR) analysis of TOCNs and hydrogels

The raw materials, viz. TOCNs, SA, AA and produced ASC hydrogels with and without TOCNs were analyzed with FT-IR spectrophotometer (VERTEX 70, Bruker, Germany) from an accumulation of 32 scans within the absorbance range of 4000 ~ 400 cm^{-1} with a resolution of 4 cm^{-1}. Prior to the tests, all samples were dried in a vacuum oven (DZF-6012, Shanghai Yiheng, P.R. China) at 40 °C for 24 h in order to remove water in the samples, and then ground to powder. The powder samples were then mixed with KBr (weight ratio about 1:100) and pressed into KBr-sheet for FT-IR analysis.

Determination of morphology of hydrogels

The morphology of AS and ASC hydrogels was determined by scanning electron microscopy with an energy-dispersive spectrometer (SEM–EDS, Zeiss, Merlin, Germany). Before observation, all hydrogel samples were freeze-dried (FDu-1200, EYELA, Japan), and then sputter-coated with a thin gold layer to avoid electron charging effects.

Transparency of hydrogels

UV–vis spectrophotometry (UV–Vis, Cary 60, Agilent, USA) was applied to determine the transparency

of AS and ASC hydrogel samples. The wavelength was 400 ~ 800 nm, and the thickness of the samples was around 4.0 mm.

Mechanical characterization of hydrogels

Before testing, the hydrogels were gently tapped on a dry, soft tissue paper to remove excess moisture from their surfaces. Then, three samples were taken from each hydrogel for mechanical tests. The humidity and temperature of the testing environment were maintained at 50% and 23 °C, respectively.

A compression testing instrument (INSTRON 5565, Instron, USA) was used to investigate the compressive strength of the hydrogels at different compressive strains up to 70%. All hydrogel samples were placed in a fume hood (room temperature) for 24 h. The cube-shaped hydrogel samples (10 × 10 × 10 mm) were conditioned and placed between two compression stages with the top stage applying uniaxial compression and release along the vertical direction. The compressive strain rate was 10% s^{-1} with a load force of 0.1 ~ 5000 N. The samples were also subjected to a cyclic loading–unloading test with a maximum compressive strain of 50% for 200 consecutive cycles using the same instrument.

The same tensile testing instrument (INSTRON 5565, Instron, USA) was applied to investigate the tensile strength of the hydrogels. All dumbbell-shape hydrogel samples were placed in sealed plastic jars (room temperature) for 24 h. The hydrogel samples were then further shaped into long-strip with a length of 30 mm, a width of 10 mm and a thickness of 1.3 mm. The sample was placed between fixtures applying a stretching force at a tensile strain rate of 20 mm min^{-1} until the sample was fractured to obtain the strength of the sample. The samples were also subjected to a cyclic loading–unloading test with a maximum tensile strain of 100% for 15 consecutive cycles using the same instrument.

Swelling and water retention of hydrogels

The swelling behavior of the hydrogels was tested by immersion of vacuum oven-dried samples (40 °C, 24 h) into DI-water until the weight remained constant. The samples were taken out of the water after every 1 h and weighed after removing excess water by gently tapping the sample surfaces with dry filter paper. The swelling rate (SR, %) was thus calculated through gravimetric determination using Eq. 3:

$$SR = \left(m_t - m_0\right)/m_0 \times 100\% \tag{3}$$

where, m_0 (g) is the initial weight of the dry sample; m_t (g) is the weight of the hydrogel sample after liquid absorption.

After swelling, the hydrogel samples were placed in an environment for up to 84 h where the temperature and humidity were set as 25 °C and 45% RH, respectively, to determine the water retention rate of the hydrogels. The water retention rate (WRR, %) of the hydrogel at 3 h intervals was calculated by Eq. 4:

$$WRR = w_t/w_0 \times 100\% \tag{4}$$

where, w_0 (g) is the initial weight of the hydrogel; w_t (g) is the weight of the hydrogel after every 3 h leaving in the test environment.

Ionic conductivity of hydrogels

The ionic conductive properties of hydrogels were determined in the way of electrochemical impedance spectroscopy (EIS) with an electrochemical workstation (CHI660E, Shanghai Chenhua, P.R. China). Cubic-shape hydrogels were tailored into 10 × 10 × 4 mm before testing. The hydrogel sample was clamped between two copper sheets to assemble a sandwich structure, which was connected to the electrochemical workstation with wires to scan its impedance spectrum in the frequency range of 0.05–10^6 Hz. The ionic conductivity (σ, S/m) of the sample was calculated by Eq. 5:

$$\sigma = L/\left(R_s \times S\right) \tag{5}$$

where, L (m) is the thickness of the hydrogel sample; R_s (Ω) is the internal resistance of the hydrogel electrolyte obtained from the impedance data; S (m^2) is the effective contact area between the hydrogel sample and the copper sheets.

Result and discussion

FT-IR analysis of TOCNs

TOCNs were synthesized by converting part of the surface hydroxymethyl groups of CNCs to their carboxylic form with the TEMPO oxidant. To confirm oxidation reaction, FT-IR spectra for MCC and TOCNs are shown in Fig. 1. The FTIR spectrum of MCC shows a broad peak centered around 3340 cm^{-1} corresponding to the –OH stretching vibration of cellulose, and the peak at 2900 cm^{-1} is characteristic of –CH stretching. The peak at 1430 cm^{-1} is associated to $–CH_2$ symmetric bending, while the peak around 1200 cm^{-1} corresponds to the C–O–C asymmetric stretching vibration at the β-glycosidic linkage. A more intense band is observed for TOCNs around 1610 cm^{-1} (which was not present in the MCC spectra), which is attributed to the C=O stretching of the carbonyl of the carboxylic acid groups (Zhao et al. 2017).

Carboxyl content of TOCNs

The –COOH content of TOCNs prepared by TEMPO-mediated oxidation is shown in Table 2. The –COOH content of TOCNs increased with the addition of oxidizing agent NaClO, and the surface –COOH content increased from 0.43 to 1.02 mmol/g_{TOCNs}, with a positive correlation of the growth ratio. This indicates that with the addition of oxidant, the surface of the samples was oxidized to a greater extent, more –COOH functional groups were introduced, and the surface –COOH content of TOCNs was higher.

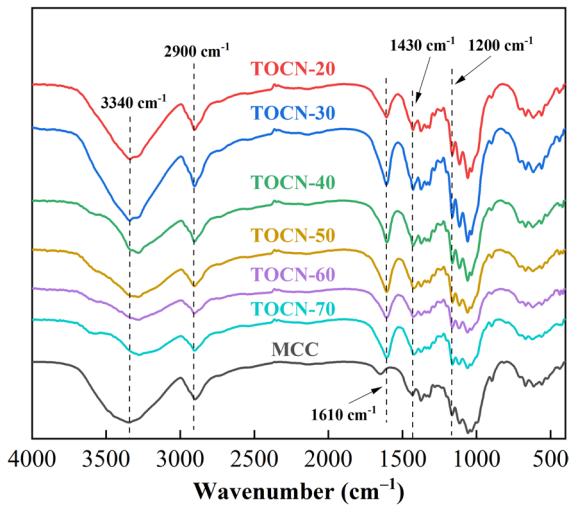

Fig. 1 FT-IR spectra of MCC and TONCs with different –COOH contents

Morphology of TOCNs

Morphological investigation of TONCs was performed by AFM observation. AFM micrographs are reported in Fig. 2a-f for the samples with different –COOH functional group contents. Typical elongated rod-like nanoparticles are observed, which diameter distribution is reported in Fig. 2g-l. No clear difference is reported for the average diameter, which value is in the range 20 ~ 23 nm, regardless of the oxidation level. The length and aspect ratio of TONCs are reported in Table 2. Cellulose significantly depolymerized during TEMPO-mediated oxidation and the length of TOCNs decreased from 710 to 380 nm when the –COOH content increased from 0.43 to 1.02 mmol/g_{TOCNs}, as also discovered elsewhere (Zhou et al. 2018). Accordingly, the aspect ratio of TOCNs decreased from 30.7 to 19.1, indicating a decrease in their dimensions. This may be beneficial for TOCNs distributed evenly in the hydrogels to play better multifunction by avoiding each other's entanglement or aggregates.

Crystallinity of TOCNs

XRD experiments were carried out to evaluate the crystallinity of TOCNs (Fig. 3). A clearly defined peak is observed at $2\theta = 22.9°$, corresponding to the crystallographic plane (200) together with less marked and broader peaks at $2\theta = 14° \sim 16°$, corresponding to planes (1–10) and (110), indicating the types of all cellulose samples were cellulose I_β. A slight rise around $2\theta = 35°$ is also observed. The peak is attributed to plane (004), which is seen to be a composite of several reflections (French 2014). It should be noted that there were two extra peaks observed at 2θ around 12.5° (1–10) and 20° (110) of MCC, which are attributed to the characteristic peaks of cellulose II (French 2014). This indicates that MCC used for producing TOCN probably contained some "contaminants"

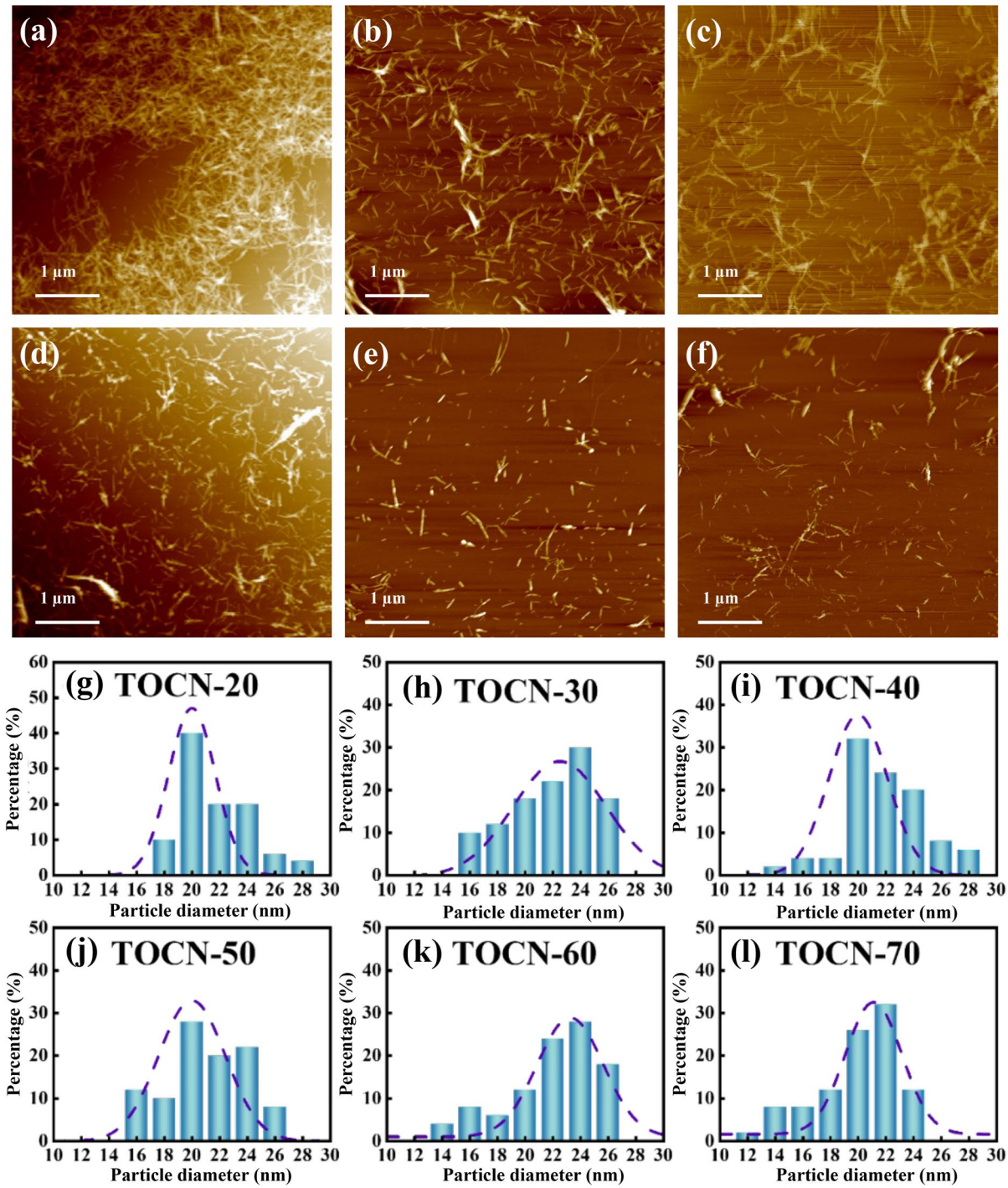

Fig. 2 AFM images (**a**-**f**), and diameter distribution (**g**-**l**) of TOCNs with different –COOH contents

(MCC-II). As the oxidation was processing, the MCC-II was dissolved and washed out (Saito and Isogai 2004), correspondingly, the two peaks disappeared gradually. However, when the strongest oxidation condition was applied, the peak at 2θ around 12.5° reappeared. This is likely due to the

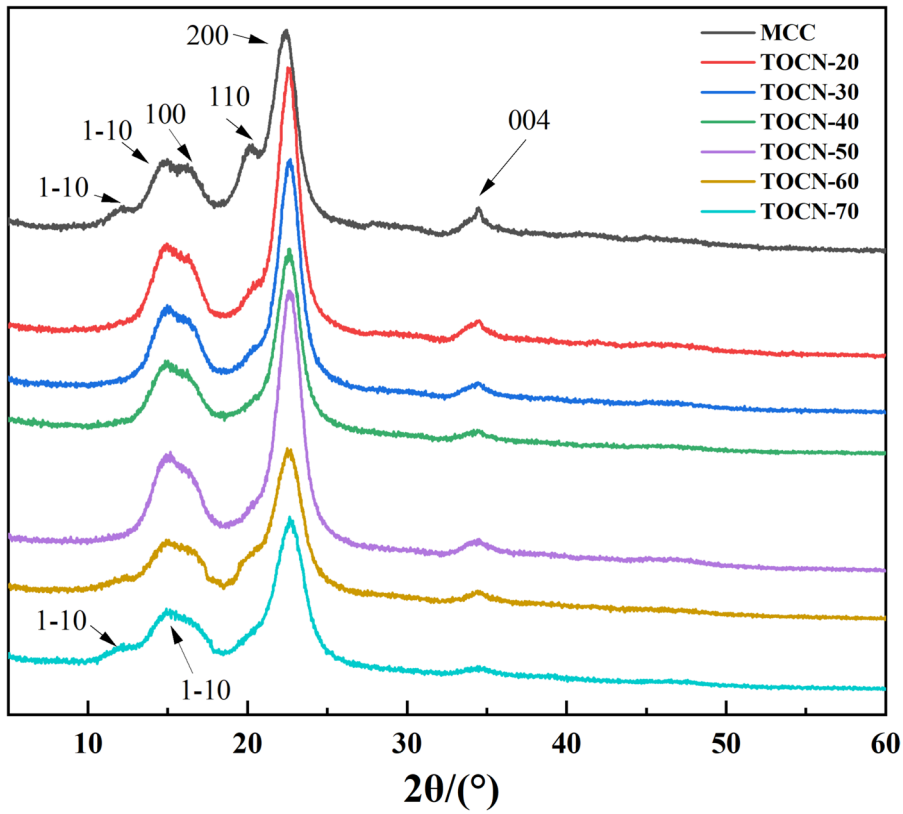

Fig. 3 XRD patterns for TOCNs with different –COOH contents

degradation of some amorphous areas of cellulose, which is co-induced by oxidation and the introduction of negative charges, resulting in a decrease in crystal size and changes in crystallites (Montanari et al. 2005). Moreover, the consumption of NaOH was the highest under this condition, which may cause oligomer recrystallisation, resulting in the presence of cellulose II.

Nevertheless, the crystallinity index is mostly unchanged after TEMPO-mediated oxidation, being about 80% for all the TOCNs. This is probably due to the oxidation occurring position-selectively at the C6–OH groups exposed on the crystalline cellulose surface (Saito and Isogai 2004; Zhou et al. 2018). This implies that the CrI of TOCNs is not a considering factor in the present study.

Zeta-potential of TOCNs and TOCN-SA suspensions

As shown in Table 2, the absolute Zeta-potentials of the TOCNs suspensions increased gradually with their –COOH contents, about 35.6 ~ 62.3 mV. This indicated that the prepared TOCNs suspensions had good dispersion stability in water owing to the increasing carboxylic group content on TOCNs, correspondingly increased the static electrical repulsion among each other. Moreover, the mixing of SA with TOCNs showed higher absolute Zeta-potential compared to the one of TOCNs suspension with the same –COOH content, which was probably caused by the introduction of more –COOH groups from SA into the mixture. The absolute Zeta-potential of SA-TOCNs also increased as the increase of –COOH contents in the TOCNs, being about 55.7 ~ 96.7 mV. Since the content of SA in all the suspensions was the same, the increase probably also resulted from the increase of –COOH contents in different TOCNs which better dispersed the SA in the mixture.

FT-IR characterization of hydrogels

The chemical structure of hydrogels was investigated by FT-IR spectroscopy to understand the interactions among AA, SA and TOCNs in the hydrogels. The characteristic peak of SA (Fig. 4a) at 3230 cm^{-1} corresponds to the stretching of –OH group, while the

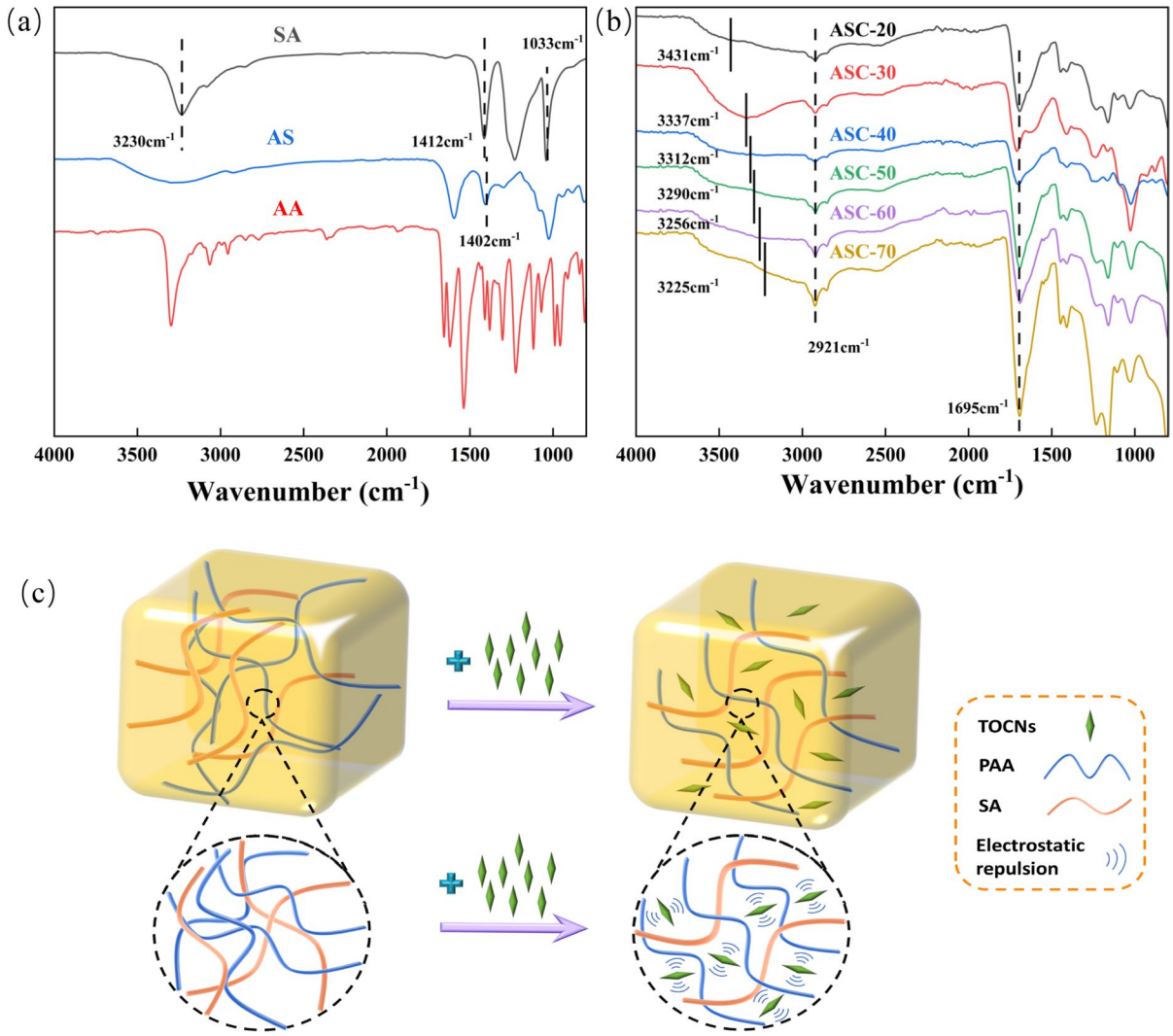

Fig. 4 **a** FT-IR spectra of raw materials; **b** Hydrogels obtained from TOCNs with different –COOH contents; and **c** Schematic illustration about the proposed semi-IPN construction of the hydrogels and the dispersing stabilizing function within the hydrogels

characteristic peak at 1412 cm^{-1} is attributed to the stretching vibration peak of the COO^- group, and the band at 1033 cm^{-1} is attributed to the stretching of C–O (Thakur et al. 2018). The characteristic peak for AS and ASC hydrogels (Fig. 4a and b) at 1402 cm^{-1} is associated to the vibration of C–N, evidencing the successful cross-linking of MBA with AA (Das et al. 2015; He et al. 2017). The appearance of the characteristic peak at 1695 cm^{-1}, which is the C=O stretching peak associated with the –COOH functional group, as well as the characteristic peak at 2921 cm^{-1} attributed to the $–CH_2$- stretching vibration, evidence the interaction between AA and SA (He et al. 2017), and the incorporation of TOCNs into the hydrogel structure (Luo et al. 2024b). Furthermore, the –OH stretching vibration peak of ASC-20 at 3431 cm^{-1} was further red-shifted to 3225 cm^{-1} in ASC-70. This is probably caused by the formation of stronger hydrogen bonding forces which can be attributed to the hydrogen bond among TOCNs, SA and PAA (Han et al. 2022).

Overall, FT-IR analysis confirmed that both SA and TOCNs permeated the PAA crosslinked network via hydrogen bonding and formed a semi-IPN structure in the hydrogel. The schematic hydrogel preparation process together with its proposed mechanism

about the semi-IPN formation of the hydrogels and dispersing stabilizing of TOCNs are illustrated on Fig. 4c. Afterwards, the morphology, transparency, mechanical properties, swelling behavior as well as ionic conductivity analysis of the hydrogels were determined in order to evaluate the effect of the semi-IPN structure and the role of TOCNs as well as its –COOH contents on the hydrogels.

Morphology of hydrogels

Incorporation of TOCNs with different –COOH contents significantly affected the network structure inside the hydrogel. It can be observed that the surface of the semi-IPN structure formed by PAA and SA was smooth and flat (Fig. 5a), with a small number and large size of internal pores, which is consistent with previously reported structures (Mao et al. 2018). In contrast, adding TOCNs makes the semi-IPN hydrogels (ASC) with many more and evenly distributed internal pores (Fig. 5b-g) because of electrostatic repulsion between TOCNs from their high –COOH content, strong enough to allow sufficient dispersion of AA and SA in the hydrogel precursor solution (Yu et al. 2016). However, different morphologies are observed depending on the oxidation level of TONCs. When initially increasing the –COOH content of TOCNs (Fig. 5b-e), the internal porosity of the hydrogel increased, pore wall gradually became thinner, while the pore radius becomes progressively larger. The internal pores gradually change from a porous to a spongy structure with high porosity, and the surface of the structure gradually becomes uneven. This can be attributed to the fact

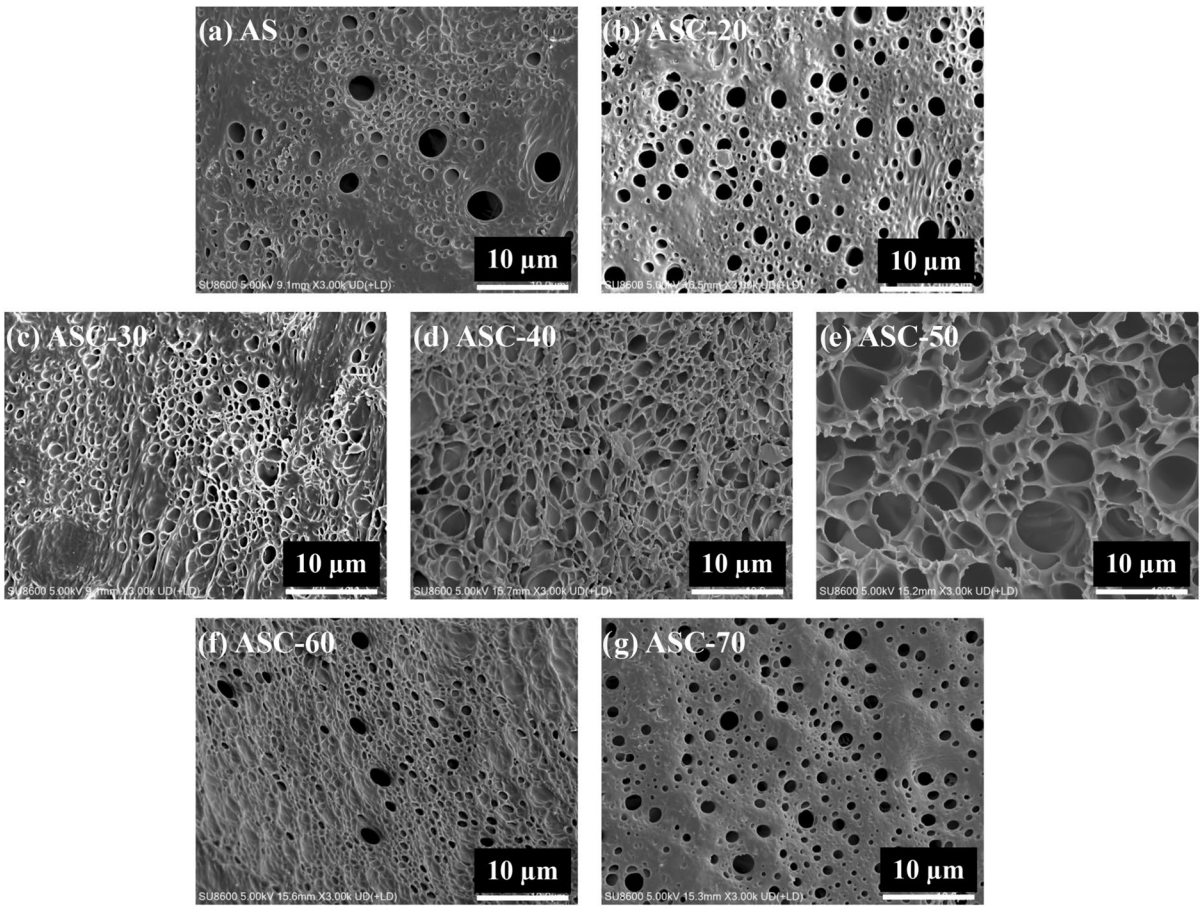

Fig. 5 SEM micrographs of hydrogels obtained from TOCNs with different –COOH contents: **a** AS; **b** ASC-20; **c** ASC-30; **d** ASC-40; **e** ASC-50; **f** ASC-60 and **g** ASC-70

that increasing –COOH content of TOCNs leads to the formation of stronger intermolecular hydrogen bonds with PAA and SA network prior to the formation of the homogeneous dispersed network structure. These stronger intermolecular hydrogen bonds affect pore formation in the hydrogel structure (Jiao et al. 2021a, b). However, ASC-60 and ASC-70 hydrogels (Fig. 5f and 5g) not only retained high porosity, but also maintained a smaller pore radius and formed a cross-sectional structure with dense pores, uniformity of pore distribution and size, and flat surface, which could exhibit better mechanical properties when exposed to external forces. SEM images show that TOCNs with high –COOH content not only provided a good dispersion effect for AA and SA, so that the hydrogels possess a homogeneous and stable structure, but also formed effective intermolecular hydrogen bonds with PAA and SA.

Mechanical properties of hydrogels

To better highlight the effect of TOCNs on the mechanical properties of PAA-SA hydrogels, a series of mechanical tests were performed. No water leakage from the hydrogels was observed during mechanical testing.

The effect of TOCNs with different –COOH contents on the compressive properties of AS and ASC hydrogels was investigated (Fig. 6a and b). As expected, introducing TOCNs into the hydrogels and increasing their –COOH content significantly

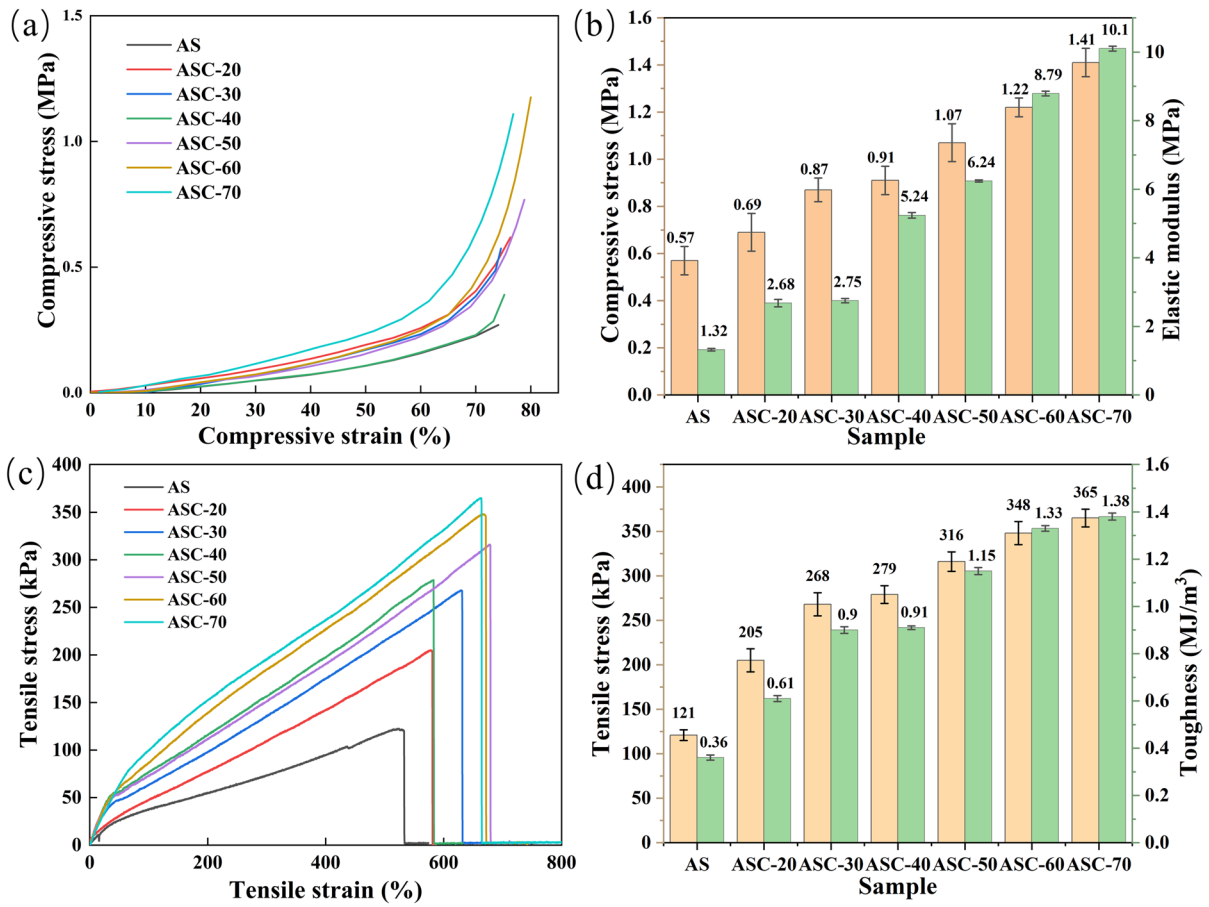

Fig. 6 **a** Compressive stress–strain curves of the cubic-shape hydrogels prepared from TOCNs with different –COOH contents; **b** Compressive stress and elastic modulus at 70% strain for hydrogels prepared from TOCNs with different –COOH contents; **c** Tensile stress–strain curves of long-strip hydrogels prepared from TOCNs with different –COOH contents at fracture strain; **d** Tensile strength and toughness for hydrogels prepared from TOCNs with different –COOH contents

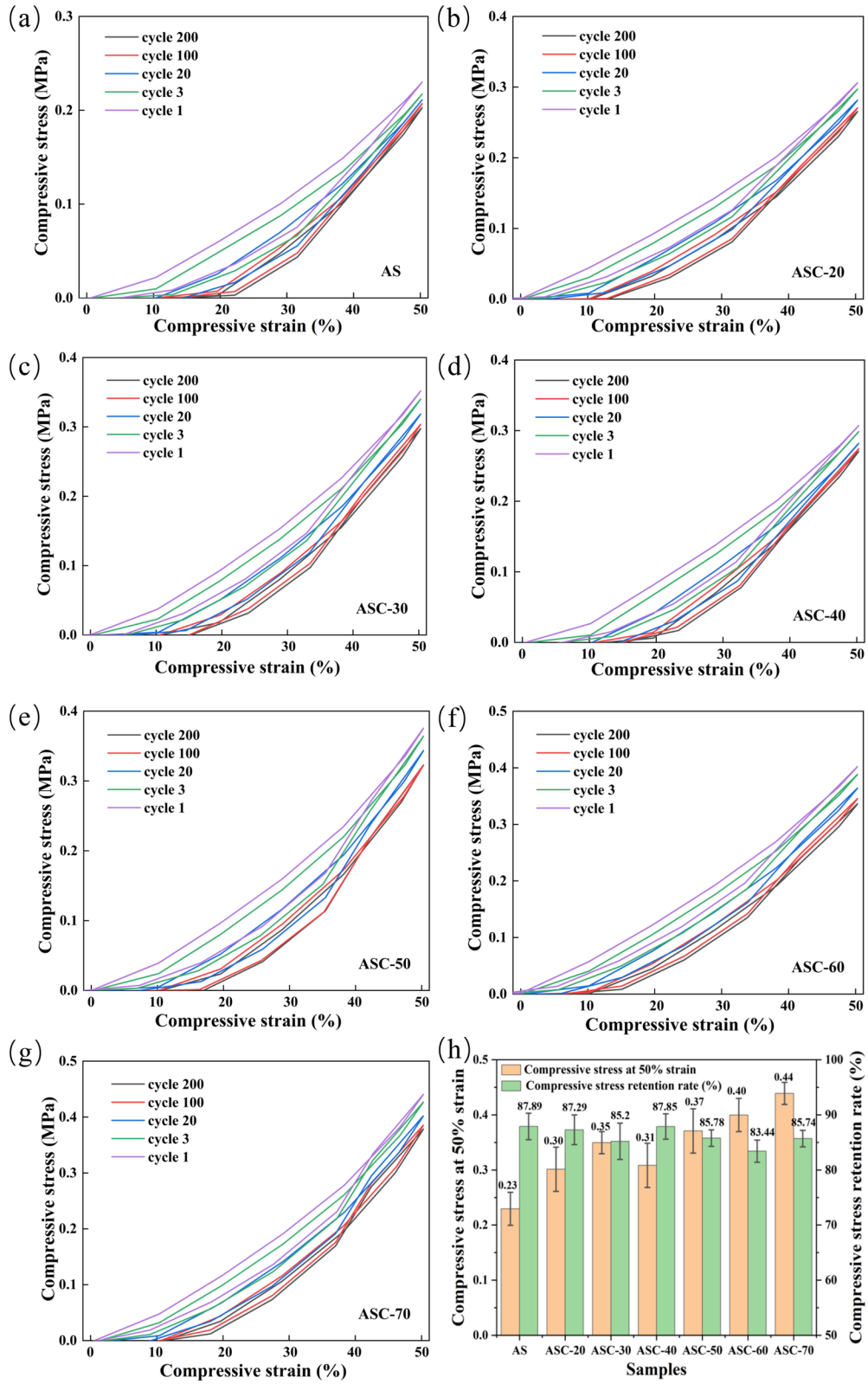
(a)
(b)
(c)
(d)
(e)
(f)
(g)
(h)
cycle 200
cycle 100
cycle 20
cycle 3
cycle 1
Compressive stress (MPa)
Compressive strain (%)
AS
ASC-20
ASC-30
ASC-40
ASC-50
ASC-60
ASC-70
Compressive stress at 50% strain
Compressive stress retention rate (%)
Samples
0.23
87.89
0.30
87.29
0.35
85.2
0.31
87.85
0.37
85.78
0.40
83.44
0.44
85.74

◂**Fig. 7** Compressive stress–strain curves for **a** AS; **b** ASC-20; **c** ASC-30; **d** ASC-40; **e** ASC-50; **f** ASC-60 and **g** ASC-70 hydrogels under 50% maximum strain for 200 loading–unloading cycles; **h** compression stress at 50% strain and compression stress retention for hydrogels prepared from TOCNs with different –COOH contents

enhanced the compressive properties of the hydrogels. For example, at 70% compressive strain, the stress (1.41 MPa) and elastic modulus (10.10 MPa) of ASC-70 were 2.47 and 7.65 times higher than those of AS (Fig. 6b), respectively. The compressive strength and elastic modulus of the hydrogels were improved to a greater extent with increasing –COOH content of TOCNs. The improvement of the compressive properties after adding TONCs to the hydrogels is due to the contribution of the high modulus of TOCNs, but also to additional and increasing hydrogen bondings (Liu et al. 2017) among TOCNs, SA and PAA in the hydrogel (Fig. 4b). Meanwhile, the addition of TOCNs and its high –COOH content also plays a key role in the homogeneous dispersion of PAA and SA.

Apart from compressive properties, the effect of TOCNs with different –COOH contents on the tensile properties of hydrogels is particularly significant, as shown in Fig. 6c and d. The toughness of the hydrogels was also estimated by calculating the area under the stress–strain curve from 0% strain to fracture strain (Morelle et al. 2018). As expected, introducing TOCNs into the hydrogels and increasing their –COOH content boosted the tensile properties of hydrogels. When TOCNs were introduced into the hydrogel, the tensile stress (365 kPa) and toughness (1.38 MJ m^{-3}) of ASC-70 hydrogel were 3.02 and 3.83 times higher than those of AS (121 kPa and 0.36 MJ m^{-3}, respectively) (Fig. 6d). This is mainly attributed to the generation of electrostatic repulsion by the high –COOH content on TOCNs, which better dispersed AA and SA in the hydrogel precursor solution for forming uniform semi-IPNs (Yu et al. 2016). This function of TOCNs was also confirmed by morphological analysis (Fig. 5).

To investigate the fatigue resistance property of hydrogels, 200 loading–unloading cycles under 50% compressive strain were performed. The results are shown in Fig. 7a-g. All curves exhibit typical deformation behavior of hydrogels, i.e., linear elastic behavior at low strain and a plastic-yielding plateau at higher strains, indicating that the materials have a stiff texture (Wieklein et al. 2015). All hydrogels exhibit the highest compressive stress in the first loading cycle, which is only slightly higher than the one for all subsequent compression cycles. All loading–unloading cycles were very similar, suggesting that all hydrogels had suitable elastic properties. In addition, similar hysteresis loops were observed for all hydrogels, indicating that they exhibit typical viscoelastic behavior in their mechanical response to compression (Zhuo et al. 2018).

All hydrogels exhibit excellent resistance to compressive fatigue, withstanding 200 compression cycles without observing slippage or fracture. After 200 compression cycles, the compressive stress retention of all hydrogels is basically at the same level, with compressive stress retention rate of 87.89% for AS hydrogel and 83.44 ~ 87.85% for ASC hydrogels (Fig. 7h). The results indicate that the improvement in fatigue resistance of hydrogels by TOCNs is limited.

Furthermore, 15 loading–unloading tensile cycles under a maximum strain of 100% were studied for all the hydrogels (Fig. 8a-g). The area under the stress–strain curve during stretching represents the total energy, and the area of the hysteresis loop represents the fraction of energy dissipated. The larger the area of the hysteresis loop, the more energy is dissipated (Liang et al. 2021). All hydrogels exhibit significant hysteresis loops, and the area of subsequent hysteresis loops are smaller than the area of the hysteresis loops for the first loading–unloading stretch. This indicates that the network inside the hydrogel has been considerably weakened upon cycling. As cycling continues, the hysteresis loop becomes smaller because the network cannot recover immediately (Yin et al. 2020; Liu et al. 2021).

All hydrogels exhibit excellent tensile fatigue resistance and were able to withstand 15 consecutive tensile cycles without slipping or fracture. The variation in tensile stress at 100% strain is consistent with the aforementioned tensile tests, where adding TOCNs and increasing –COOH content significantly increased the hydrogels' stress at 100% tensile strain (Fig. 10h). The tensile stress retention rate of AS hydrogel was 87.51%, and that of ASC hydrogels ranged from 83.37 to 92.08%, with the tensile stress retention rate of ASC-70 hydrogel reaching 92.08%. When TOCN-70 was introduced, the area of the hysteresis loop was significantly reduced, indicating

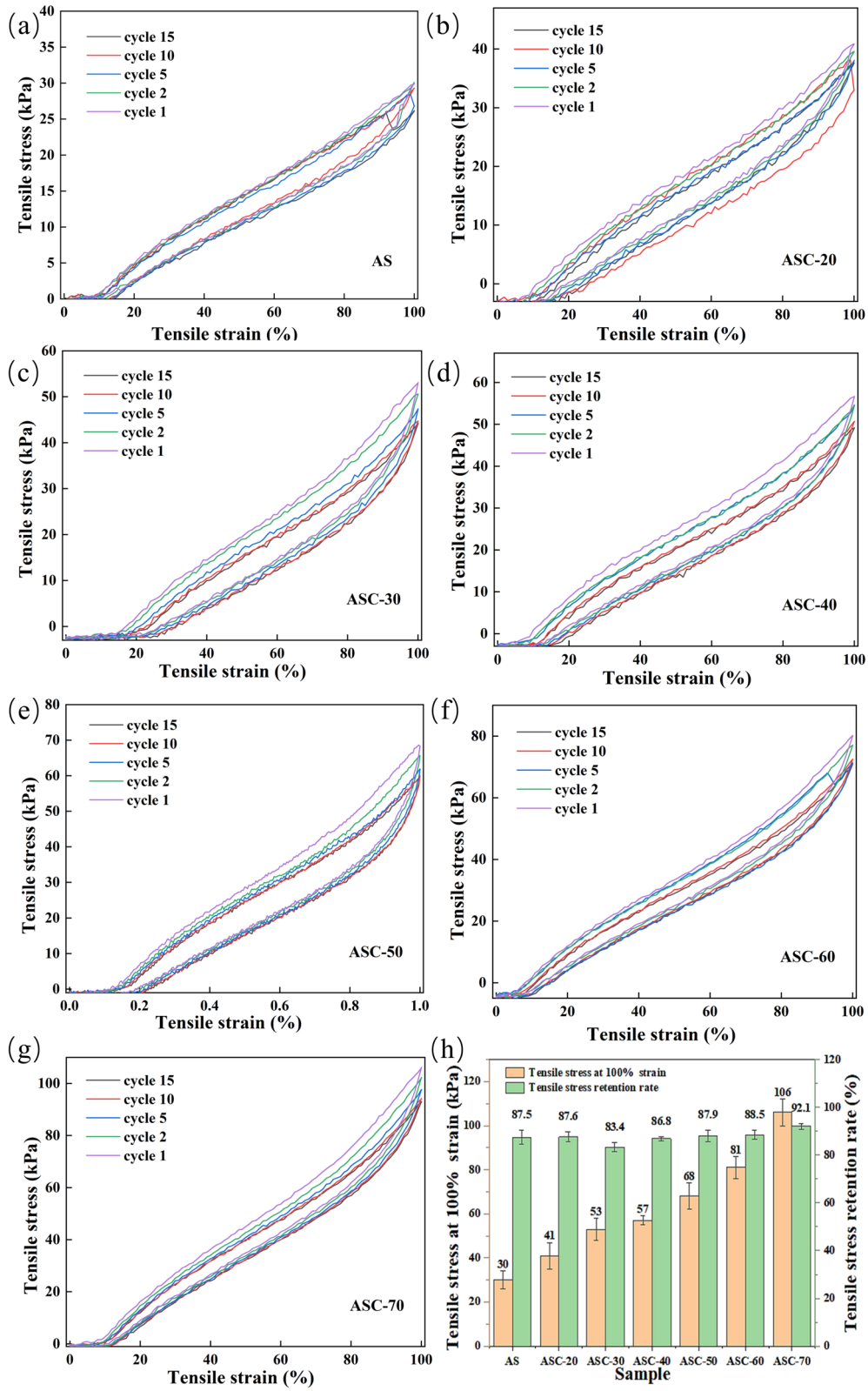
(a)
cycle 15
cycle 10
cycle 5
cycle 2
cycle 1
AS
Tensile stress (kPa)
Tensile strain (%)
(b)
ASC-20
(c)
ASC-30
(d)
ASC-40
(e)
ASC-50
(f)
ASC-60
(g)
ASC-70
(h)
Tensile stress at 100% strain
Tensile stress retention rate
Tensile stress at 100% strain (kPa)
Tensile stress retention rate (%)
Sample
30
41
53
57
68
81
106
87.5
87.6
83.4
86.8
87.9
88.5
92.1

◂**Fig. 8** Tensile stress–strain curves for **a** AS; **b** ASC-20; **c** ASC-30; **d** ASC-40; **e** ASC-50; **f** ASC-60; and **g** ASC-70 hydrogels under 100% maximum strain for 15 loading–unloading cycles; **h** Tensile stress at 100% strain and tensile stress retention for hydrogels prepared from TOCNs with different –COOH contents

that the fatigue resistance of the hydrogel has been enhanced (Ling et al. 2021).

At last, it is worth mentioning that the aspect ratio of TOCNs decreased for TOCN-20 ~ TOCN-70, which was supposed to have a negative effect on the mechanical properties of the hydrogels. However, the results showed that the addition of TOCNs and its increase in –COOH contents (TOCN-20 ~ TOCN-70) improved the mechanical properties of the hydrogels. This, on the other hand, further confirms the key roles of –COOH contents in TOCNs played in the hydrogels.

Transparency of hydrogels

Transparency is an important feature for hydrogels. A highly transparent hydrogel allows light to pass through without causing excessive light scattering or absorption, which can make the hydrogel to efficiently receive optical energy and convert it into electrical energy in the photoelectricity conversion device, offering a wide range of applications in the field of photoelectricity (Go et al. 2023; Kong et al. 2023). All hydrogels with a thickness of around 4 mm exhibit high transmittance in the 400 ~ 800 nm wavelength range, as determined by UV–Vis spectrometry (Fig. 9a). Compared to AS, ASC hydrogels with high –COOH content TOCNs show higher transmittance, indicating that the hydrogels have better transparency. However, the average transmittance of AS at 700 ~ 800 nm is 72.7% (Fig. 9b), and the transmittance of ASC-20 and ASC-30 is 65.8% and 69.3%, respectively, indicating that AA and SA were not evenly distributed in the hydrogel network structure with a small amount of TOCNs, resulting in a loss of light transmission (Li et al. 2017). When further increasing the –COOH content of TOCNs, the transparency of ASC was significantly enhanced. Light transmittance at 700 ~ 800 nm finally increased from 79.4 to 86.3%, indicating that high –COOH content of TOCNs led to a more homogeneous dispersion of SA and AA in the system, and formed a more homogeneous and porous network structure, which promoted light transmission through the network structure (Tong et al. 2019). This agrees with SEM imaging (Fig. 5).

Conductivity of hydrogels

From the hydrogels´ internal resistance (R_s), measured by the EIS method, the ionic conductivity was calculated to evaluate the performance of the conductive hydrogels prepared in this work. Two identical copper sheets and the hydrogel were assembled into a sandwich structure for measurement (Fig. 9c). Generally, the EIS spectrum consists of a semicircle in the high-frequency region and a straight line in the low-frequency region. The downward-sloping area in the low-frequency region indicates the capacitance characteristics, and the intersection of the semicircle with the real axis in the medium–high frequency region indicates hydrogel resistance. As shown in Fig. 9c, all hydrogels have R_s lower than 700 Ω, which is attributed to the presence of –COOH on AA, SA and TOCNs that dissociate in water, conferring a conductive property to hydrogels. The addition of TOCNs to the hydrogel and the increase of –COOH contents of TOCNs increased the number of ions, resulting in a reduction in R_s for most ASCs hydrogels compared to AS hydrogel. Adding TOCNs increased the conductivity of ASC hydrogel, the value reaching about 0.229 S m^{-1} (Fig. 9d). This demonstrates the contribution of –COOH groups of TOCNs to hydrogel conductivity.

Swelling and water retention of hydrogels

The ability of hydrogels to swell and retain water is very important for their applications, especially for drug release and dye adsorption (Thakur et al. 2018). Figure 10a and b show the swelling curves of AS and ASC hydrogels as well as the swelling rate after 48 h conditioning at 45% RH. It can be observed that the swelling rate of all hydrogel samples is time-dependent. All hydrogels showed excellent water absorption ability and swelled rapidly at the early stage. All hydrogels swelled faster during the first 24 h because the initial hydrogel samples are rich in internal pores (as shown in Fig. 5), which can rapidly absorb a large amount of water. After 24 h, the hydrogels' internal pores are filled with a large amount of water, resulting in a slowdown in the swelling rate. After 48 h, the

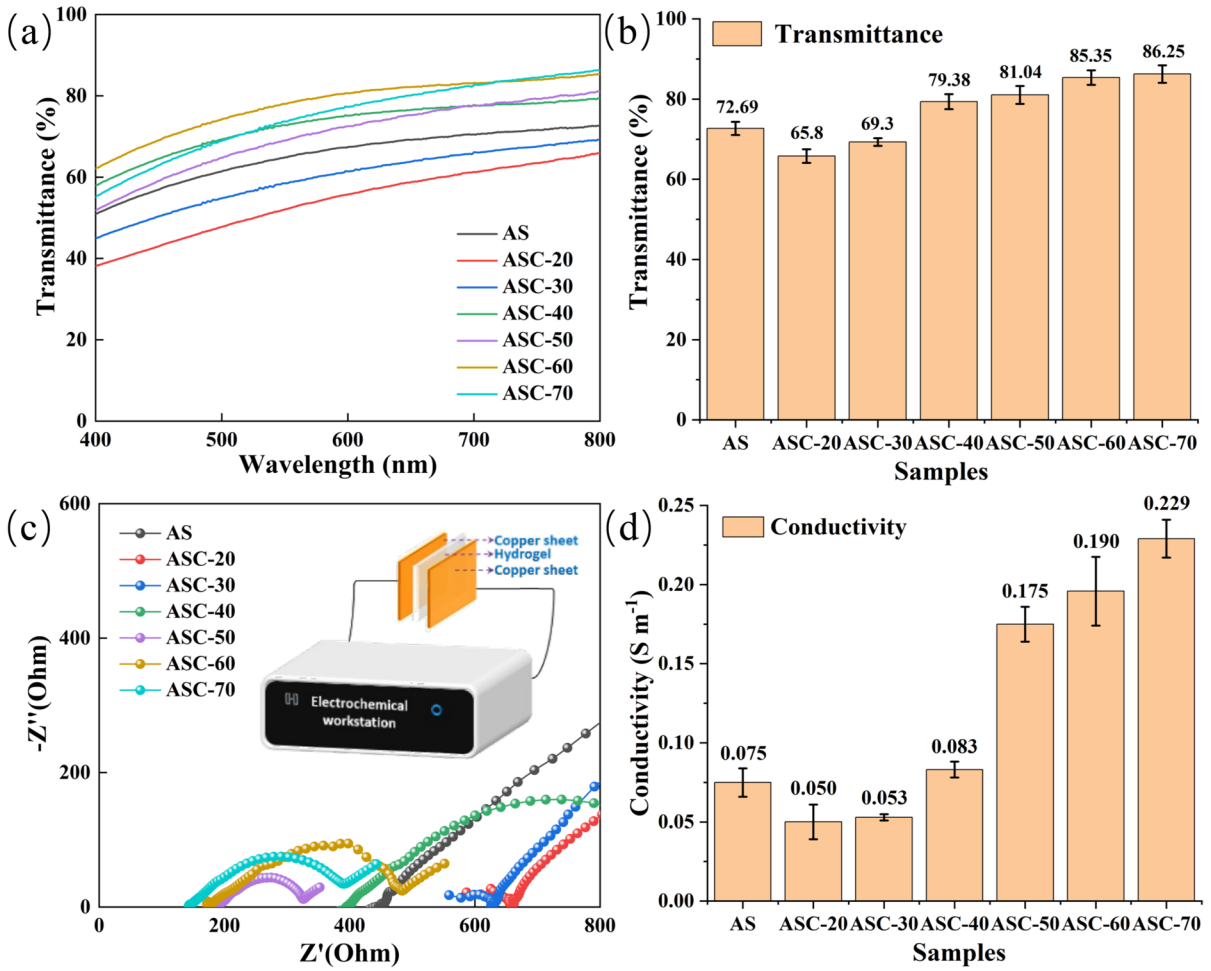

Fig. 9 **a** Light transmittance of hydrogels in the wavelength range 400 ~ 800 nm; **b** Average transmittance of hydrogels at 700 ~ 800 nm; **c**, **d** EIS and corresponding conductivity for hydrogels as well as schematic diagram of the assembly for the EIS test

swelling rate for AS hydrogel exceeded 2100% and further increased with the addition of TOCNs and its –COOH content increase, being up to 2509% (ASC-70), indicating excellent water absorption and swelling ability (Table S1) as well as the importance of TOCNs in them.

Conventional hydrogels retain water poorly due to easy evaporation of water at the hydrogel interface, which has important implications for their practical application (Sui et al. 2021). Therefore, the water retention property of hydrogels was investigated (Fig. 10c) by measuring the mass change rate of hydrogels against time up to 84 h. Hydrogel mass decreased rapidly over the first 36 h and slowly between 36 and 84 h. The final water retention of all hydrogels is rather similar, with an average value of 53.5% (Fig. 10d), indicating that all hydrogels have good water retention properties (Sui et al. 2021). However, a small improvement in water retention of the hydrogels can be noted with increasing –COOH content of the TOCNs.

Overall, considering the mechanical stresses, conductivity, swelling and water retention properties of the hydrogel ASC-70, most of them are competitive compared to most of the PAA-based conductive hydrogels reported in nearly 4 years (Table S1), indicating that the TOCNs' multifunctioning in PAA-SA hydrogels is an effective strategy to improve the properties of PAA-SA hydrogels.

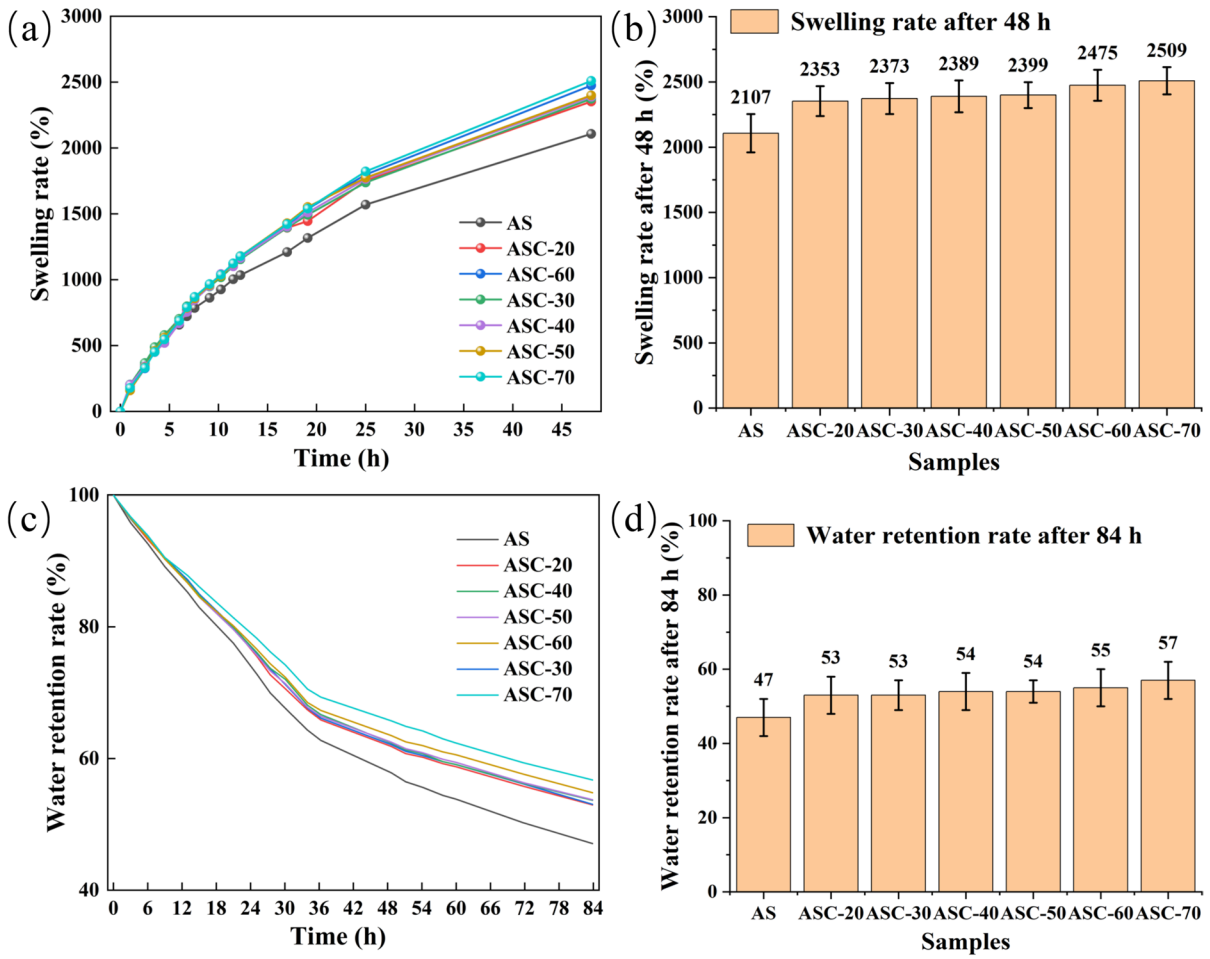

Fig. 10 **a**, **b** Swelling rate over time, and **c**, **d** Water retention over time for hydrogels prepared from TOCNs with different –COOH contents

Conclusions

In this work, cellulose nanocrystals with different –COOH contents (TOCNs) were prepared by TEMPO-oxidation method, and were successfully applied for preparing PAA-SA hydrogels. The multifunctional roles that the TOCNs played in the hydrogel included well-dispersing SA and AA in the hydrogel precursor solution to form a uniform semi-IPN network, providing more hydrogen bonds with SA and AA, and offering high modulus to the final hydrogel. These efficiently improved both the mechanical and conductive properties of the hydrogel. The as-prepared hydrogel therefore had excellent compressive properties (1.41 MPa at compressive strain of 70%) and tensile properties (365 kPa at fracture strain of 628%). It also showed excellent compressive fatigue-resistant properties (strength retention up to 87.85% after 200 cycles of compression), tensile fatigue-resistant properties (tensile strength retention up to 92.08% after 15 cycles of 100% stretching), high swelling rate (exceeding 2100%), good transparency (up to 86.3%) and conductivity (up to 0.229 S m^{-1}). Considering that all the raw materials used have good natural biocompatibility, the prepared hydrogels show great potential for applications in the fields of biomedicine, flexible wearable sensors and environmental governance.

Acknowledgements We appreciate greatly the financial supports from the Foundation of State Key Laboratory of Biobased Material and Green Papermaking, Qilu University of

Technology, Shandong Academy of Sciences (GZKF202123), Taishan Scholars Program of Shandong Province, and the Project to Attract Foreign Experts by MOST (G2023163006L and H20250222). LGP2 is part of the LabEx Tec 21 (Investissements d'Avenir—grant agreement n°ANR-11-LABX-0030) and of the PolyNat Carnot Institut (Investissements d'Avenir—grant agreement n°ANR-11-CARN-030-01). Special thanks to Prof. Yoshiharu Nishiyama from CERMAV-CNRS and Benoît Duchemin from Le Havre University for their valuable knowledge support to XRD.

Author contribution Tao Song: Conceptualization, Methodology, Formal analysis, Investigation, Resources, Writing-original draft, Writing-Reviewing & Editing, Funding acquisition, Visualization; Qiang Wang: Investigation, Visualization, Funding acquisition; Tingting Han: Conceptualization, Methodology, Supervision, Resources, Writing-Reviewing & Editing; Alain Dufresne, Fernanda Andrade Tigre da Costa and Duclerc Fernandes Parra: Resources, Writing-Reviewing & Editing, Funding acquisition.

Funding The Foundation of State Key Laboratory of Biobased Material and Green Papermaking,Qilu University of Technology, Shandong Academy of Sciences, GZKF202123, GZKF202123, the Project to Attract Foreign Experts by MOST, G2023163006L, G2023163006L, H20250222, H20250222, Taishan Scholars Program of Shandong Province, the LabEx Tec 21, n°ANR-11-LABX-0030, n°ANR-11-LABX-0030, n°ANR-11-LABX-0030, the PolyNat Carnot Institut, n°ANR-11-CARN-030-01, n°ANR-11-CARN-030-01, n°ANR-11-CARN-030-01.

Data availability No datasets were generated or analysed during the current study.

Declarations

Conflict of interest The authors declare that they have no known competing financial interests or personal relationships that could have appeared to influence the work reported in this paper.

References

Aminabhavi TM, Nadagouda MN, More UA, Joshi SD, Kulkarni VH, Noolvi MN, Kulkarni PV (2015) Controlled release of therapeutics using interpenetrating polymeric networks. Expert Opin Drug Deliv 12(4):669–688. https://doi.org/10.1517/17425247.2014.974871

Bandodkar AJ, Molinnus D, Mirza O, Guinovart T, Windmiller JR, Valdes-Ramirez G, Wang J (2014) Epidermal tattoo potentiometric sodium sensors with wireless signal transduction for continuous non-invasive sweat monitoring. Biosens Bioelectron 54:603–609. https://doi.org/10.1016/j.bios.2013.11.039

Barbash VA, Yashchenko OV, Gondovska AS, Deykun IM (2022) Preparation and characterization of nanocellulose obtained by TEMPO-mediated oxidation of organosolv pulp from reed stalks. Appl Nanosci 12(4):835–848. https://doi.org/10.1007/s13204-021-01749-z

Brannon-Peppas L, Harland RS (1990) Absorbent polymer technology. Elsevier Science, The Netherlands

Buwalda SJ, Boere KWM, Dijkstra PJ, Feijen J, Vermonden T, Hennink WE (2014) Hydrogels in a historical perspective: from simple networks to smart materials. J Control Release 190:254–273. https://doi.org/10.1016/j.jconrel.2014.03.052

Cen Y, Xiang ZY, Han TT, Long Y, Song T (2022) Effect of microfluidizing cycles after citric acid hydrolysis on the production yield and aspect ratio of cellulose nanocrystals. Cellulose 29:7193–7209. https://doi.org/10.1007/s10570-022-04725-0

Chen Q, Zhu L, Chen H, Yan H, Huang L, Yang J, Zheng J (2015) A novel design strategy for fully physically linked double network hydrogels with tough, fatigue resistant, and self-healing properties. Adv Funct Mater 25(10):1598–1607. https://doi.org/10.1002/adfm.201404357

Chen YY, Lu KY, Song YH, Han JQ, Yue YY, Biswas SK, Wu QL, Xiao HN (2019) A skin-inspired stretchable, self-healing and electro-conductive hydrogel with a synergistic triple network for wearable strain sensors applied in human-motion detection. Nanomaterials 9(12):1737. https://doi.org/10.3390/nano9121737

Chen GQ, Huang JR, Gu JF, Peng SJ, Xiang XT, Chen K, Yang XX, Guan LH, Jiang XC, Hou LX (2020) Highly tough supramolecular double network hydrogel electrolytes for an artificial flexible and low-temperature tolerant sensor. J Mater Chem A 8(14):6776–6784. https://doi.org/10.1039/D0TA00002G

Daniele MA, Adams AA, Naciri J, North SH, Ligler FS (2014) Interpenetrating networks based on gelatin methacrylamide and PEG formed using concurrent thiol click chemistries for hydrogel tissue engineering scaffolds. Biomaterials 35(6):1845–1856. https://doi.org/10.1016/j.biomaterials.2013.11.009

Das D, Ghosh P, Dhara S, Panda AB, Pal S (2015) Dextrin and poly(acrylic acid)-based biodegradable, non-cytotoxic, chemically cross-linked hydrogel for sustained release of ornidazole and ciprofloxacin. ACS Appl Mater Interfaces 7(8):4791–4803. https://doi.org/10.1021/am508712e

Dashtebayaz MSS, Nourbakhsh MS (2019) Interpenetrating networks hydrogels based on hyaluronic acid for drug delivery and tissue engineering. Int J Polym Mater Polym Biomater 68(8):442–451. https://doi.org/10.1080/00914037.2018.1455680

De Koker S, Cui JW, Vanparijs N, Albertazzi L, Grooten J, Caruso F, De Geest BG (2016) Engineering polymer hydrogel nanoparticles for lymph node-targeted delivery. Angewandte Chemie-International Edition 55(4):1334–1339. https://doi.org/10.1002/anie.201508626

Dhand AP, Galarraga JH, Burdick JA (2021) Enhancing biopolymer hydrogel functionality through interpenetrating networks. Trends Biotechnol 39(5):519–538. https://doi.org/10.1016/j.tibtech.2020.08.007

Dragan ES (2014) Design and applications of interpenetrating polymer network hydrogels. A review. Chem Eng J 243:572–590. https://doi.org/10.1016/j.cej.2014.01.065

Draget KI, Taylor C (2011) Chemical, physical and biological properties of alginates and their biomedical implications. Food Hydrocolloids 25(2):251–256. https://doi.org/10.1016/j.foodhyd.2009.10.007

Fan JC, Shi ZX, Wang JL, Yin J (2013) Glycidyl methacrylate-modified gum arabic mediated graphene exfoliation and its use for enhancing mechanical performance of hydrogel. Polymer 54(15):3921–3930. https://doi.org/10.1016/j.polymer.2013.05.057

Fang W, Song T, Wang LS, Han TT, Xiang ZY, Rojas OJ (2023) Influence of formic acid esterified cellulose nanofibrils on compressive strength, resilience and thermal stability of polyvinyl alcohol-xylan hydrogel. Carbohydr Polym 308:120663. https://doi.org/10.1016/j.carbpol.2023.120663

French AD (2014) Idealized powder diffraction patterns for cellulose polymorphs. Cellulose 21:885–896. https://doi.org/10.1007/s10570-013-0030-4

Go Y, Park H-Y, Zhu Y, Yoo K, Kwak J, Jin S-H, Yoon J (2023) Optically transparent and mechanically robust ionic hydrogel electrodes for bright electroluminescent devices achieving high stretchability over 1400%. Adv Funct Mater 33(32):2215193. https://doi.org/10.1002/adfm.202215193

Godiya CB, Cheng X, Li D, Chen Z, Lu X (2019) Carboxymethyl cellulose/polyacrylamide composite hydrogel for cascaded treatment/reuse of heavy metal ions in wastewater. J Hazard Mater 364:28–38. https://doi.org/10.1016/j.jhazmat.2018.09.076

Gong JP, Katsuyama Y, Kurokawa T, Osada Y (2003) Double-network hydrogels with extremely high mechanical strength. Adv Mater 15(14):1155–1158. https://doi.org/10.1002/adma.200304907

Guo S, Zhu Y, Xu W, Huan S, Li J, Song T, Rojas OJ (2023) Heteroaggregation effects on Pickering stabilization using oppositely charged cellulose nanocrystal and nanochitin. Carbohydr Polym. https://doi.org/10.1016/j.carbpol.2022.120154

Hamad W (2006) On the development and applications of cellulosic nanofibrillar and nanocrystalline materials. Can J Chem Eng 84(5):513–519. https://doi.org/10.1002/cjce.5450840501

Han T, Song T, Pranovich A, Rojas OJ (2022) Engineering a semi-interpenetrating constructed xylan-based hydrogel with superior compressive strength, resilience, and creep recovery abilities. Carbohydr Polym 294:119772. https://doi.org/10.1016/j.carbpol.2022.119772

Hao X, Li N, Wang H, Jia S, Liu Q, Peng F (2021) Dialdehyde xylan-based sustainable, stable, and catalytic liquid metal nano-inks. Green Chem 23(19):7796–7804. https://doi.org/10.1039/D1GC02696H

He G, Ke W, Chen X, Kong Y, Zheng H, Yin Y, Cai W (2017) Preparation and properties of quaternary ammonium chitosan-g-poly(acrylic acid-co-acrylamide) superabsorbent hydrogels. React Funct Polym 111:14–21. https://doi.org/10.1016/j.reactfunctpolym.2016.12.001

Ho TC, Chang CC, Chan HP, Chung TW, Shu CW, Chuang KP, Duh TH, Yang MH, Tyan YC (2022) Hydrogels: properties and applications in biomedicine. Molecules 27(9):2902. https://doi.org/10.3390/molecules27092902

Isogai A, Saito T, Fukuzumi H (2011) TEMPO-oxidized cellulose nanofibers. Nanoscale 3:71–85. https://doi.org/10.1039/C0NR00583E

Jeong JO, Park JS, Kim EJ, Jeong SI, Lee JY, Lim YM (2020) Preparation of radiation cross-linked poly(acrylic acid) hydrogel containing metronidazole with enhanced antibacterial activity. Int J Mol Sci 21(1):187. https://doi.org/10.3390/ijms21010187

Ji H, Xiang ZY, Qi HS, Han TT, Pranovich A, Song T (2019) Strategy towards one-step preparation of carboxylic cellulose nanocrystals and nanofibrils with high yield, carboxylation and highly stable dispersibility using innocuous citric acid. Green Chem 21:1956–1964. https://doi.org/10.1039/C8GC03493A

Jiao Y, Lu Y, Lu KY, Yue YY, Xu XW, Xiao HN, Li J, Han JQ (2021a) Highly stretchable and self-healing cellulose nanofiber-mediated conductive hydrogel towards strain sensing application. J Colloid Interface Sci 597:171–181. https://doi.org/10.1016/j.jcis.2021.04.001

Jiao Y, Lu K, Lu Y, Yue Y, Xu X, Xiao H, Li J, Han J (2021b) Highly viscoelastic, stretchable, conductive, and self-healing strain sensors based on cellulose nanofiber-reinforced polyacrylic acid hydrogel. Cellulose 28(7):4295–4311. https://doi.org/10.1007/s10570-021-03782-1

Joshi R, Friedrich J, Krishna-Subramanian S (2013) Surface modification of ultra-high molecular weight polyethylene membranes using underwater plasma polymerization. Plasma Chem Plasma Process 33(5):921–940. https://doi.org/10.1007/s11090-013-9476-2

Ke FY, Zhang QK, Ji LY, Zhang YY, Zhang CX, Xu J, Chen Y (2021) Electrostatic adhesion of polyaniline on carboxylated polyacrylonitrile fabric for high-performance wearable ammonia sensor. Compos Commun 27:100817. https://doi.org/10.1016/j.coco.2021.100817

Kobayashi Y, Saito T, Isogai A (2014) Aerogels with 3D ordered nanofiber skeletons of liquid-crystalline nanocellulose derivatives as tough and transparent insulators. Angewandte Chemie-International Edition 53(39):10394–10397. https://doi.org/10.1002/anie.201405123

Koehler J, Wallmeyer L, Hedtrich S, Goepferich AM, Brandl FP (2017) Ph-modulating poly(ethylene glycol)/alginate hydrogel dressings for the treatment of chronic wounds. Macromol Biosci 17(5):1600369. https://doi.org/10.1002/mabi.201600369

Kong WQ, Wang CW, Jia C, Kuang YD, Pastel G, Chen CJ, Chen GG, He SM, Huang H, Zhang JH, Wang S, Hu LB (2018) Muscle-inspired highly anisotropic, strong, ion-conductive hydrogels. Adv Mater 30(39):1801934. https://doi.org/10.1002/adma.201801934

Kong L, Yuan Z, Sun N, Ding J, Liu S, Zhang S, Lv Z, Xu W, Liu G, Liu X (2023) Advances in flexible hydrogels for light-thermal-electricity energy conversion and storage. J Energy Storage 60:106618. https://doi.org/10.1016/j.est.2023.106618

Li SF, Wang HL, Huang WD, Liu XL (2014) Facile preparation of pH-sensitive poly(acrylic acid-co-acrylamide)/SiO2 hybrid hydrogels with high strength by in situ frontal polymerization. Colloid Polym Sci 292(1):107–113. https://doi.org/10.1007/s00396-013-3050-6

Li RA, Chen G, He M, Tian J, Su B (2017) Patternable transparent and conductive elastomers towards flexible tactile/strain sensors. J Mater Chem C 5(33):8475–8481. https://doi.org/10.1039/C7TC02703F

Li X, Li J, Gong J, Kuang Y, Mo L, Song T (2018) Cellulose nanocrystals (CNCs) with different crystalline allomorph for oil in water pickering emulsions. Carbohydr Polym 183:303–310

Li SH, Pan HY, Wang YT, Sun JQ (2020) Polyelectrolyte complex-based self-healing, fatigue-resistant and anti-freezing hydrogels as highly sensitive ionic skins. J Mater Chem A 8(7):3667–3675. https://doi.org/10.1039/C9TA13213A

Li IC, Chen Y-H, Chen Y-C (2022) Sodium alginate-g-poly(sodium acrylate) hydrogel for the adsorption-desorption of ammonium nitrogen from aqueous solution. J Water Process Eng 49:102999. https://doi.org/10.1016/j.jwpe.2022.102999

Liang Y, Shen Y, Sun X, Liang H (2021) Preparation of stretchable and self-healable dual ionically cross-linked hydrogel based on chitosan/polyacrylic acid with anti-freezing property for multi-model flexible sensing and detection. Int J Biol Macromol 193:629–637. https://doi.org/10.1016/j.ijbiomac.2021.10.060

Lin F, Lu X, Wang Z, Lu Q, Lin G, Huang B, Lu B (2019) In situ polymerization approach to cellulose-polyacrylamide interpenetrating network hydrogel with high strength and pH-responsive properties. Cellulose 26(3):1825–1839. https://doi.org/10.1007/s10570-018-2171-y

Ling QJ, Ke T, Liu WT, Ren ZJ, Zhao L, Gu HB (2021) Tough, repeatedly adhesive, cyclic compression-stable, and conductive dual-network hydrogel sensors for human health monitoring. Ind Eng Chem Res 60(50):18373–18383. https://doi.org/10.1021/acs.iecr.1c03358

Ling QJ, Liu WT, Liu JC, Zhao L, Ren ZJ, Gu HB (2022) Highly sensitive and robust polysaccharide-based composite hydrogel sensor integrated with underwater repeatable self-adhesion and rapid self-healing for human motion detection. ACS Appl Mater Interfaces 14(21):24741–24754. https://doi.org/10.1021/acsami.2c01785

Liu YJ, Cao WT, Ma MG, Wan PB (2017) Ultrasensitive wearable soft strain sensors of conductive, self-healing, and elastic hydrogels with synergistic "soft and hard" hybrid networks. ACS Appl Mater Interfaces 9(30):25559–25570. https://doi.org/10.1021/acsami.7b07639

Liu XY, Liu J, Lin ST, Zhao XH (2020) Hydrogel machines. Mater Today 36:102–124. https://doi.org/10.1016/j.mattod.2019.12.026

Liu JL, Ai J, Chen JW, Guo Y, Lin JR, Chen QH (2021) Adhesive, self-healing, conductive Janus gel with oil-water responsiveness. Colloids Surf B Biointerfaces 207:112028. https://doi.org/10.1016/j.colsurfb.2021.112028

Luo YC, Song T, Ji H, Qi HS, Xiang ZY, Xiong HP, Cen Y, Chen G, Han TT, Pranovich A (2021) Preliminary investigations of the mechanisms involved in the ultrasonication-assisted production of carboxylic cellulose nanocrystals with different structural carboxylic acids. ACS Sustain Chem Eng 9:4531–4542. https://doi.org/10.1021/acssuschemeng.0c08929

Luo J, Song T, Han T, Qi H, Liu Q, Rosenau T (2024a) Multifunctional roles of TEMPO-oxidized cellulose nanofibrils on the enhancement of mechanical and conductive properties of acrylic-based hydrogels for temperature response and human motion sensing. Chem Eng J 493:152649. https://doi.org/10.1016/j.cej.2024.152649

Luo J, Song T, Han T, Qi H, Liu Q, Wang Q, Song Z, Rojas O (2024b) Multifunctioning of carboxylic-cellulose nanocrystals on the reinforcement of compressive strength and conductivity for acrylic-based hydrogel. Carbohydr Polym 327:121685. https://doi.org/10.1016/j.carbpol.2023.121685

Maleki L, Edlund U, Albertsson A-C (2016) Green semi-IPN hydrogels by direct utilization of crude wood hydrolysates. ACS Sustain Chem Eng 4(8):4370–4377. https://doi.org/10.1021/acssuschemeng.6b00938

Mao X, Wang L, Gu S, Duan Y, Zhu Y, Wang C, Lichtfouse E (2018) Synthesis of a three-dimensional network sodium alginate-poly(acrylic acid)/attapulgite hydrogel with good mechanic property and reusability for efficient adsorption of Cu^{2+} and Pb^{2+}. Environ Chem Lett 16(2):653–658. https://doi.org/10.1007/s10311-018-0708-9

Montanari S, Roumani M, Heux L, Vignon MR (2005) Topochemistry of carboxylated cellulose nanocrystals resulting from TEMPO-mediated oxidation. Macromolecules 38(5):1665–1671. https://doi.org/10.1021/ma048396c

Morelle XP, Illeperuma WR, Tian K, Bai R, Suo Z, Vlassak JJ (2018) Highly stretchable and tough hydrogels below water freezing temperature. Adv Mater 30(35):1801541. https://doi.org/10.1002/adma.201801541

Mougel JB, Adda C, Bertoncini P, Capron I, Cathala B, Chauvet O (2016) Highly efficient and predictable noncovalent dispersion of single-walled and multiwalled carbon nanotubes by cellulose nanocrystals. J Phys Chem C 120(39):22694–22701

Pinelli F, Magagnin L, Rossi F (2020) Progress in hydrogels for sensing applications: a review. Mater Today Chem 17:100317. https://doi.org/10.1016/j.mtchem.2020.100317

Qiao HY, Qi PF, Zhang XH, Wang LA, Tan YQ, Luan ZH, Sui KY (2019) Multiple weak H-bonds lead to highly sensitive, stretchable, self-adhesive, and self-healing ionic sensors. ACS Appl Mater Interfaces 11(8):7755–7763. https://doi.org/10.1021/acsami.8b20380

Saito T, Isogai A (2004) TEMPO-mediated oxidation of native cellulose. The effect of oxidation conditions on chemical and crystal structures of the water-insoluble fractions. Biomacromol 5:1983–1989. https://doi.org/10.1021/bm0497769

Schazmann B, Morris D, Slater C, Beirne S, Fay C, Reuveny R, Moyna N, Diamond D (2010) A wearable electrochemical sensor for the real-time measurement of sweat sodium concentration. Anal Methods 2(4):342–348. https://doi.org/10.1039/B9AY00184K

Shi XC, Wang ZB, Liu SY, Xia QQ, Liu YZ, Chen WS, Yu HP, Zhang K (2024) Scalable production of carboxylated cellulose nanofibres using a green and recyclable solvent. Nat Sustain 7:315–325. https://doi.org/10.1038/s41893-024-01267-0

Sui XJ, Guo HS, Cai CC, Li QS, Wen CY, Zhang XY, Wang XD, Yang J, Zhang L (2021) Ionic conductive hydrogels with long-lasting antifreezing, water retention and

self-regeneration abilities. Chem Eng J 419:129478. https://doi.org/10.1016/j.cej.2021.129478

Tang J, Shi Z, Berry RM, Tam KC (2015) Mussel-inspired green metallization of silver nanoparticles on cellulose nanocrystals and their enhanced catalytic reduction of 4-nitrophenol in the presence of β-cyclodextrin. Ind Eng Chem Res 54(13):3299–3308

Thakur S, Arotiba OA (2018) Synthesis, swelling and adsorption studies of a pH-responsive sodium alginate-poly(acrylic acid) superabsorbent hydrogel. Polym Bull 75(10):4587–4606. https://doi.org/10.1007/s00289-018-2287-0

Tong R, Chen G, Pan D, Qi H, Li RA, Tian J, Lu F, He M (2019) Highly stretchable and compressible cellulose ionic hydrogels for flexible strain sensors. Biomacromol 20(5):2096–2104. https://doi.org/10.1021/acs.biomac.9b00322

Wang T, Zhang Y, Liu QC, Cheng W, Wang XR, Pan LJ, Xu HX (2018) A self-healable, highly stretchable, and solution processable conductive polymer composite for ultrasensitive strain and pressure sensing. Adv Funct Mater 28(7):1705551. https://doi.org/10.1002/adfm.201705551

Wang LS, Song T, Cen Y, Qi HS, Han TT (2025) Effects of physical properties of nanocellulose crystals on dispersion of carbon nanotubes and properties of their composite membranes. Fine Chem 42(2):332–344. https://doi.org/10.13550/j.jxhg.20240035

Wichterle O, Lim D (1960) Hydrophilic gels for biological use. Nature 185:117–118. https://doi.org/10.1038/185117a0

Wicklein B, Kocjan A, Salazar-Alvarez G, Carosio F, Camino G, Antonietti M, Bergstrom L (2015) Thermally insulating and fire-retardant lightweight anisotropic foams based on nanocellulose and graphene oxide. Nat Nanotechnol 10(3):277–283. https://doi.org/10.1038/nnano.2014.248

Wieduwild R, Krishnan S, Chwalek K, Boden A, Nowak M, Drechsel D, Werner C, Zhang Y (2015) Noncovalent hydrogel beads as microcarriers for cell culture. Angewandte Chemie-International Edition 54(13):3962–3966. https://doi.org/10.1002/anie.201411400

Xiao GF, Fu SY, Lucia LA (2021) Poly(aminobenzeneboronic acid)-mediated rapid self-healing and shape memory cellulose crystal nanohydrogels. Carbohydr Polym 255:117495. https://doi.org/10.1016/j.carbpol.2020.117495

Xu D, Huang J, Zhao D, Ding B, Zhang L, Cai J (2016) High-flexibility, high-toughness double-cross-linked chitin hydrogels by sequential chemical and physical cross-linkings. Adv Mater 28(28):5844–5849. https://doi.org/10.1002/adma.201600448

Yang JA, Yeom J, Hwang BW, Hoffman AS, Hahn SK (2014) In situ-forming injectable hydrogels for regenerative medicine. Prog Polym Sci 39(12):1973–1986. https://doi.org/10.1016/j.progpolymsci.2014.07.006

Yin J, Pan S, Wu L, Tan L, Chen D, Huang S, Zhang Y, He P (2020) A self-adhesive wearable strain sensor based on a highly stretchable, tough, self-healing and ultra-sensitive ionic hydrogel. J Mater Chem C 8(48):17349–17364. https://doi.org/10.1039/D0TC04144K

Yu HY, Zhang DZ, Lu FF, Yao JM (2016) New approach for single-step extraction of carboxylated cellulose nanocrystals for their use as adsorbents and flocculants. ACS Sustain Chem Eng 4(5):2632–2643. https://doi.org/10.1021/acssuschemeng.6b00126

Zhang HJ, Sun TL, Zhang AK, Ikura Y, Nakajima T, Nonoyama T, Kurokawa T, Ito O, Ishitobi H, Gong JP (2016) Tough physical double-network hydrogels based on amphiphilic triblock copolymers. Adv Mater 28(24):4884–4890. https://doi.org/10.1002/adma.201600466

Zhang C, Wu BH, Zhou YS, Zhou F, Liu WM, Wang ZK (2020) Mussel-inspired hydrogels: from design principles to promising applications. Chem Soc Rev 49(11):3605–3637. https://doi.org/10.1039/C9CS00849G

Zhang Y, Li MY, Han X, Fan ZW, Zhang HH, Li QL (2021) High-strength and highly electrically conductive hydrogels for wearable strain sensor. Chem Phys Lett 769:138437. https://doi.org/10.1016/j.cplett.2021.138437

Zhao F, Repo E, Song Y, Yin D, Ben Hammouda S, Chen L, Kalliola S, Tang J, Tam KC, Sillanpää M (2017) Polyethylenimine-cross-linked cellulose nanocrystals for highly efficient recovery of rare earth elements from water and a mechanism study. Green Chem 19:4816–4828. https://doi.org/10.1039/C7GC01770G

Zhou Y, Saito T, Bergström L, Isogai A (2018) Acid-free preparation of cellulose nanocrystals by TEMPO oxidation and subsequent cavitation. Biomacromol 19(2):633–639. https://doi.org/10.1021/acs.biomac.7b01730

Zhuo H, Hu YJ, Tong X, Chen ZH, Zhong LX, Lai HH, Liu LX, Jing SS, Liu QZ, Liu CF, Peng XW, Sun RC (2018) A supercompressible, elastic, and bendable carbon aerogel with ultrasensitive detection limits for compression strain, pressure, and bending angle. Adv Mater 30(18):1706705. https://doi.org/10.1002/adma.201706705